

Algorithms and radiation dynamics for the vicinity of black holes

II. Results

Leela Elpida Koutsantoniou

Department of Astrophysics, Astronomy and Mechanics, Faculty of Physics, University of Athens, Panepistimiopolis Zografos, Athens 15784, Greece
e-mail: leelamk@phys.uoa.gr

Received 21 June 2022 / Accepted 18 January 2023

ABSTRACT

We present the results of our studies on accretion disks in proximity to astrophysical black holes. These disks can be of varying degrees of opacity, geometrical shapes, size and volume. The central compact object is a Schwarzschild or a Kerr black hole of assorted spin parameters. We describe the environment and the physics of the systems under examination and the disk models considered. We first investigate the effects of the spacetime rotation on photon trajectories. We then examine the radiation forces recorded in various points of the arrangement inside and outside the disk material, and in inner, outer and off-equatorial material orbits. We thus document and explore the radiation effects that are revealed to be significant and positively not inconsequential. Afterward, we inspect the possible imaging outcome of various types of black hole and accretion disk configurations. Subsequently, we show our results for plots that could be used to estimate the central black hole spin in a system. Finally, we show results about the disk material orbit degradation due to its thermal radiation.

Key words. accretion, accretion disks – black hole physics – magnetic fields – radiative transfer – relativistic processes

1. Introduction

Black hole observation and research has marked considerable advances in recent years. Making use of technological developments, new ground instruments are constructed and state-of-the-art space programs are designed in order to observe and record these perplexing objects and their peculiar environment. Even instruments not intended for black hole observation are often used for such a purpose, since they can document the effects of secondary phenomena originating from a compact object and its system. These can then frequently provide information about the object under study and its properties.

The mass M for a stellar mass black hole, hereafter BH, is estimated to range approximately between 5 and 100 Solar masses (e.g., Hughes 2005¹). In most cases, we observe stellar mass BHs surrounded by accretion disks, henceforth ADs, for longer or shorter periods of time. These times depend on the configuration setup and the greatly varying accreting mass quantity, usually ranging from a few days to a few hundreds of days, (see e.g., Lasota 2016). We have thus turned our attention to such systems and investigate the assorted radiation effects encountered in strong gravity environments examining their properties and the radiation impact.

The temperature of ADs of this type is fairly high ($T \sim 10^7\text{K}$) and causes the emission of X-rays at $E \sim 1\text{keV}$ or higher (Zhang et al. 1997; Kylafis et al. 2012). The presence of these noncentral sources of light brings into play dynamical effects that modify the equilibrium and shape the evolution of the disk. The primary goal of our research was to study the

Poynting–Robertson (PR) effect (Poynting 1903; Larmor 1917; Page 1918; Robertson 1937) in BH and AD systems. We would then evaluate its ramifications in these setups and assess the importance of the induced effects. This phenomenon is noteworthy because it creates a drag force onto the disk material. Thereupon, the material slowly brakes, falls further inward and finally accretes onto the central compact object. The nature of strong gravity environments, however, has proven to set in motion a series of more complicated and entangled effects that require proper physical treatment.

In the first part of this work (Koutsantoniou 2022) we explained the theoretical formulation and the equations required in order to study the problem. We also described the AD models we used in this study. Additionally, we presented the codes written and used for this research and gave an account of their capabilities. In this second part, we show and explain the results of the various facets of our study and discuss their implications. We begin by investigating the ramifications of the spacetime curvature and its effects on photon trajectories. We then examine the recorded radiation forces on the AD material for various models and spin parameters. We should also keep in mind here that these radiation forces depend on the target velocity and hence have distinct consequences on particles of different velocity profiles. We thus consider the significance and the importance of the disk material characteristics. Further on, we investigate our BH-AD imaging capabilities and examine what additional information can be drawn from this for the systems. Finally, we discern the subsequent effects of the radiation pressure on massive particle trajectories.

Some of the first and perhaps most fundamental steps in the study of radiation in the vicinity of massive objects were taken by Abramowicz, Ellis, & Lanza (1990), Miller & Lamb (1993,

¹ The lower limit for BH mass, the Tolman–Oppenheimer–Volkoff limit is still under active research, see Bombaci (1996); Kalogera & Baym (1996); Thompson et al. (2019); Abbott et al. (2020), but also Jayasinghe et al. (2021) and El-Badry et al. (2022).

1996) and Lamb & Miller (1995). These groups studied the radiation of a central star reaching points of the environment and presented analytical formulae that calculate the radiation field in these less complicated, perhaps, conditions. Subsequently, we also mention the noteworthy studies presented in Fuerst & Wu (2004, 2007) and Wu et al. (2008a,b), where radiation, radiative transfer, and emission lines in proximity to BHs were surveyed assiduously. In addition to the above, we should also mention the relevant work presented in Younsi et al. (2012) and Younsi (2014) that extended the aforementioned studies. Furthermore, thorough research on the numerous and intricate aspects of radiation in strong gravity was conducted by Bini et al. (2009, 2011a,b, 2015), where a notable number of intriguing subjects were demonstrated and examined.

Finally, we should mention that this study was initiated in order to better examine the Cosmic Battery (Contopoulos & Kazanas 1998; Contopoulos et al. 2006, 2009) and evaluate its effects onto ADs around BHs. In this process the hot disk orbiting the BH radiates thermally due to its high temperature ($T \gtrsim 10^7 \text{K}$, $E \gtrsim 1 \text{keV}$, see e.g., Kylafis et al. 2012). This radiation is then absorbed by the disk material itself, exerting radiation forces influenced by the aforementioned Poynting–Robertson effect. The radiation, nonetheless, primarily affects the material electrons since $f_e/f_p \sim (m_p/m_e)^2$, where f_p and f_e the force on a proton and on an electron and m_p , m_e are their masses, respectively. The consequence of this is the electrons moving with a lower speed than the protons and thus the generation of a ring current. This ring current then in turn generates a poloidal magnetic field in the system. The presence of a growing and expanding magnetic field in this environment has further effects and implications. These include, for example, the Blandford–Znajek process (Blandford & Znajek 1977; Livio et al. 1999; Komisarov 2001; McKinney 2005) which induces the extraction of energy from the BH. All these new physical components and circumstances then lead to different structural forms and equilibrium conditions in the entire configuration, which should be investigated anew.

The best environments where such situations and phenomena can be examined are systems of binary stars that include one typical “donor” star (main sequence star, red giant or white dwarf) and one “accretor” compact star (neutron star or BH). These X-ray binary systems are illuminated due to matter transference from the more gas-rich companion to the compact component. During this process, matter is stripped off the companion star’s external layers and creates a short-lived AD around the compact object (e.g., Lasota 2016). This reconfiguration compels the infalling matter to release its gravitational potential energy and emit it as luminous energy in the band of X-rays. Abundant theoretical and observational information concerning these intriguing arrangements can be found for instance in Podsiadlowski et al. (2002); Tauris & van den Heuvel (2006); Belloni (2010a,b,c); Kylafis et al. (2012); Tetarenko et al. (2016). Considering the X-ray binaries’ evolutionary sequence, periodicity, and variability timescales we can find detailed information for the various different situations in van der Klis & Bonnet-Bidaud (1989); van der Klis (1995, 2004); Uttley et al. (2005); Koljonen et al. (2010); Reig & Fabregat (2015); Reig et al. (2016); Lasota (2016).

Finally, before concluding this Sect. we should mention some of the notable observational studies that provided valuable information for our own and numerous other related researches. These include observations made using Very-long-baseline interferometry (VLBI; e.g., Zavala & Taylor 2003; Taylor & Zavala 2010), Very Long Baseline Array (VLBA; e.g.,

Zavala & Taylor 2002, 2003, 2004, 2005; Taylor & Zavala 2010), Monitoring Of Jets in Active galactic nuclei with VLBA Experiments (MOJAVE; e.g., Hovatta et al. 2012, 2014), Hubble Space Telescope (HST; e.g., Tsvetanov et al. 1999), Very Large Array (VLA; e.g., Zavala & Taylor 2002, 2004; Herrnstein et al. 2005; Carilli & Taylor 2002; Krause & Löhr 2004; Govoni et al. 2010), Chandra (e.g., Kronberg et al. 2001 and references therein), INTErnational Gamma-Ray Astrophysics Laboratory (INTEGRAL) & Swift (e.g., Bonafede et al. 2010 and references therein), Röntgensatellit (ROSAT; e.g., Widrow 2002), X-ray Multi-Mirror Mission (XMM-Newton; e.g., Widrow 2002 and references therein), Skinakas Observatory (SKO; e.g., Reig & Fabregat 2015; Reig et al. 2016), Event Horizon Telescope (EHT, e.g., M87: Event Horizon Telescope Collaboration 2019a,b,c, 2021a,b, Sgr A*: Event Horizon Telescope Collaboration 2022a,b,c,d). Finally yet importantly, we should mention here studies that combine a multitude of the aforementioned observatories and instruments in order to examine phenomena closely related and very useful for our research. Some of these are Gabuzda et al. (2004, 2008, 2012, 2014, 2015a,b); Gabuzda (2006, 2015); Mahmud & Gabuzda (2007, 2008, 2009); Mahmud et al. (2009); Contopoulos et al. (2009); O’Sullivan & Gabuzda (2009); Reichstein & Gabuzda (2012); Murphy et al. (2013); Mahmud et al. (2013); Murphy & Gabuzda (2013); Christodoulou et al. (2016).

In the present work, we start in Sect. 2 by setting up the problem: we show the Kerr metric and its notable surfaces, the general relativistic radiative transfer equation and its solution, and the AD models we used. Subsequently, in Sect. 3 we demonstrate the results of our studies: photon trajectories in strong gravity, radiation forces and dynamics, BH imaging at infinity and its capabilities, and massive particle trajectories in strong gravity under the influence of radiation pressure. Finally, in Sect. 4 we summarize our results and discuss their implications.

2. Setting up the problem

2.1. The Kerr metric and notable surfaces

We assume that the immediate environment around a potentially rotating and accreting BH can be adequately described using the Kerr metric (Kerr 1963; Bardeen et al. 1972). The setup’s spacetime can thus be determined by the central compact object that is axisymmetric, uncharged and possibly rotating. Additionally, we assume that the presence and motion of test particles does not affect the spacetime form or the stress–energy tensor. We henceforth use the geometrized unit system, where $c = G = 1$ and distances are measured in units of gravitational radii $r_g = GM/c^2 = M$, where M is the BH mass. We also assume the Einstein notation for summation over double indices. We denote spacetime components by Greek indices and space components by Latin indices.

We can fully describe the BH and the spacetime around it using its mass M and spin parameter a . The spin parameter a takes values from $a = 0$ for a nonrotating Schwarzschild BH to $a = M$ for a maximally rotating one. Alternatively, we may use $j = 0$ and $j = 1$ respectively, for the dimensionless angular momentum $j = a/M$. The Kerr metric in Boyer–Lindquist coordinates (t, ϕ, r, θ) , hereafter BL, is then given by:

$$\begin{aligned} ds^2 &= g_{\alpha\beta} dx^\alpha dx^\beta \\ &= -e^{2\nu} dt^2 + e^{2\psi} (d\phi - \omega dt)^2 + e^{2\mu_1} dr^2 + e^{2\mu_2} d\theta^2, \end{aligned} \quad (1)$$

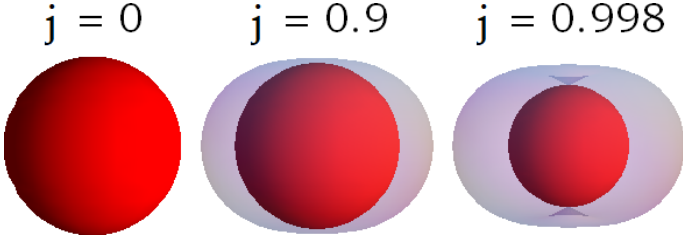


Fig. 1: Event horizon in red and ergosphere in gray of a BH with various angular momentum values. The ergosphere starts in low j as an ellipsoid, turning into a spindle torus for high j . We also notice the shrinkage of the event horizon for increasing values of j .

where:

$$e^{2\nu} = \frac{\Sigma\Delta}{A}, \quad e^{2\psi} = \frac{A\sin^2\theta}{\Sigma}, \quad e^{2\mu_1} = \frac{\Sigma}{\Delta}, \quad e^{2\mu_2} = \Sigma, \quad (2)$$

with:

$$\Delta = r^2 - 2Mr + a^2,$$

$$\Sigma = r^2 + a^2\cos^2\theta,$$

$$A = (r^2 + a^2)^2 - a^2\Delta\sin^2\theta, \quad (3)$$

and the spacetime angular velocity is given by:

$$\omega = -\frac{g_{\phi t}}{g_{\phi\phi}} = \frac{2Mra}{A}, \quad (4)$$

see [Bardeen \(1970\)](#) and [Bardeen, Press, & Teukolsky \(1972\)](#).

From the metric (1) we determine assorted notable surfaces around a rotating BH. The BH outer event horizon firstly stems from one of the poles of the g_{rr} component and can be found at the outermost root of the equation $\Delta = 0$:

$$r_{\text{evh}} = M + \sqrt{M^2 - a^2}. \quad (5)$$

The event horizon has hence the shape of a sphere with radius $r_{\text{evh}} = 2M$ for a nonrotating Schwarzschild BH and with $r_{\text{evh}} = M$ for a maximally rotating one.

The next notable surface is the static limit that establishes the outer boundary surface of the ergosphere. The static limit is found at the point where the g_{tt} metric component changes sign, namely for radius:

$$r_{\text{ergo}} = M + \sqrt{M^2 - a^2\cos^2\theta}. \quad (6)$$

For a Schwarzschild BH, the ergosphere is a sphere with radius $r_{\text{ergo}} = 2M$, the Schwarzschild radius. For increasing values of a , the ergosphere turns into an oblate spheroid with an equatorial (maximum) radius $r_{\text{ergo}}^{\theta=\pi/2} = 2M$ and a polar (minimum) radius $r_{\text{ergo}}^{\text{polar}} = r_{\text{evh}}$. Lastly, for a maximal BH, the ergosphere approximates a spindle torus² (Fig. 1). From the above, we deduce that the ergosphere may change its shape for increasing a , yet it maintains a constant equatorial radius and a decreasing radius

² A spindle torus is a three-dimensional geometrical shape that is produced by the rotation of a circle around an axis in the same plane as the circle. The distance of this axis from the center of the circle is smaller than the circle radius. Objects approximating a spindle torus is an apple and a pumpkin.

in the poles, where it always remains in contact with the event horizon. Inside this static limit, we have that $g_{tt} < 0$. This forces any particle moving there, massive or massless, to corotate with the BH with at least $\omega = -g_{\phi t}/g_{\phi\phi}$, so that its proper time τ remains positive. Finally, we also note that in theory it is possible to extract energy and mass from this region around the BH via the Penrose process ([Penrose & Floyd 1971](#)).

Another mentionable surface around the BH is the innermost circular equatorial orbit for particles. The limiting case is the one describing particle motion with infinite energy per unit mass. This is the photon orbit, the innermost equatorial circular orbit for any particle. The radius of the photon orbit is given by:

$$r_{\text{ph}} = 2M \left\{ 1 + \cos \left[\frac{2}{3} \cos^{-1} \left(\mp \frac{a}{M} \right) \right] \right\}, \quad (7)$$

where the upper sign refers to direct (corotating with the BH) and the lower sign to retrograde (counter-rotating) orbits. For a Schwarzschild BH ($a = 0$), the photon orbit radius is $r_{\text{ph}} = 3M$ and for a maximally rotating BH ($a = M$), the radii are $r_{\text{ph}} = M$ for the direct and $r_{\text{ph}}^{\text{retro}} = 4M$ for the retrograde photon ring.

Finally, we mention the innermost stable circular orbit for massive particles of the disk, hereafter ISCO. The radius of the ISCO is given by:

$$r_{\text{ISCO}} = M \left[3 + Z_2 \mp \sqrt{(3 - Z_1)(3 + Z_1 + 2Z_2)} \right], \quad (8)$$

where:

$$Z_1 = 1 + \left(1 - \frac{a^2}{M^2} \right)^{1/3} \left[\left(1 + \frac{a}{M} \right)^{1/3} + \left(1 - \frac{a}{M} \right)^{1/3} \right],$$

$$Z_2 = \sqrt{\frac{3a^2}{M^2} + Z_1^2}, \quad (9)$$

where again the upper sign in Eq. (8) refers to direct orbits and the lower sign to retrograde orbits. The ISCO radius is hence $r_{\text{ISCO}} = 6M$ for $a = 0$. For $a = M$, the direct ISCO has radius $r_{\text{ISCO}} = M$ and the retrograde ISCO has radius $r_{\text{ISCO}}^{\text{retro}} = 9M$.

The values and evolution of the radius of these notable surfaces for all spin parameters can be seen in Fig. 2. For $a/M = 0$ we have a spherically symmetric object for all the surfaces. For $a/M > 0$, we see the radius of the direct orbits and for $a/M < 0$, the radius of the retrograde orbits. We should also note here that, even though the aforementioned characteristic surfaces appear to coincide at radius $r = M$ for a maximally rotating BH, in reality they do not. This is a false appearance, caused by the structure of the Boyer–Lindquist coordinate system. These metric solutions are distinct for any spin a and differ in radial proper distance (e.g., [Bardeen et al. 1972](#); [Chandrasekhar 1983](#)).

Along with the aforementioned notable orbits and surfaces, there are also other such important structures. These include, for example, the marginally bound massive particle orbit with radius $r_{\text{mb}} = 2M \mp a + 2\sqrt{M(M \mp a)}$ and the inner horizon or ergosphere. Since we will not be using any of these, however, the reader can look for instance into [Bardeen, Press, & Teukolsky \(1972\)](#) or [Misner, Thorne, & Wheeler \(1973\)](#) for more information.

Before moving along we also mention the coordinate angular velocity for a circular equatorial orbit, that is given by:

$$\Omega = \frac{d\phi}{dt} = \frac{u^\phi}{u^t} = \frac{M^{1/2}}{r^{3/2} + aM^{1/2}}, \quad (10)$$

where $u^\alpha = (u^t, u^\phi, u^r, u^\theta)$ is the four-velocity of a particle.

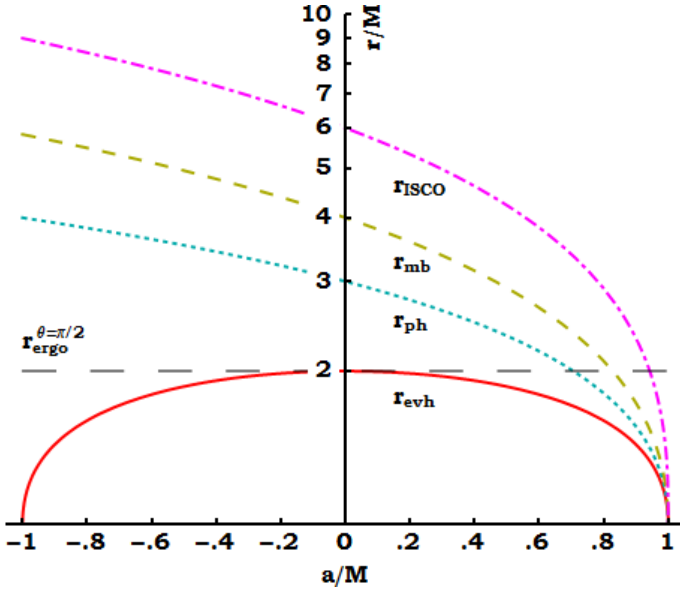


Fig. 2: Radii of the notable equatorial orbits. In addition to the surfaces we use and we mention in Sect. 2.1, we also include for completeness the marginally bound circular orbit radius r_{mb} .

2.2. Radiative transfer

In this subsection we discuss the radiative transfer equation (RTE) and its general relativistic form (GRRTE). Thermal radiation is emitted from the hot AD and can have temperatures of 10^7 K or more, high enough to produce X-rays. This radiation spreads in the system and is absorbed by the disk material itself, material in possible outflow regions, escaping material propelled by winds or even material stationary above the disk. The radiation specific intensity I_ν ($\text{erg s}^{-1} \text{cm}^{-2} \text{ster}^{-1} \text{Hz}^{-1}$) is thus adjusted and redefined depending on the trajectory it follows and the material it interacts with. Namely, the radiation has its magnitude increased as the trajectory passes through the hot and emitting disk material. At the same time, the intervening material absorbs part of the radiation, decreasing its intensity. Depending on this material's density and abundance, the light ray may manage to traverse the interceding material or else is absorbed along the way.

In classical environments (see Rybicki & Lightman 1986), the RTE for the specific intensity I_ν at frequency ν (Hz) takes the form:

$$I_\nu(s) = I_\nu(s_0) e^{-\tau_\nu} + \int_{s_0}^s j_\nu(s') e^{-[\tau_\nu(s) - \tau_\nu(s')]} ds', \quad (11)$$

where the optical depth τ_ν (dimensionless quantity) is given by:

$$\tau_\nu(s) = \int_{s_0}^s a_\nu(s') ds' \quad (12)$$

and the absorption coefficient a_ν (cm^{-1}) by:

$$a_\nu = n\sigma_\nu, \quad (13)$$

with σ_ν (cm^2) the absorbing area cross section at frequency ν and n (cm^{-3}) the material number density. Lastly, we have the emission coefficient j_ν ($\text{erg cm}^{-3} \text{s}^{-1} \text{ster}^{-1} \text{Hz}^{-1}$) that is given by:

$$j_\nu = \frac{dI_\nu}{ds}. \quad (14)$$

In the above equations, s stands for the classically measured path length.

When, nonetheless, we wish to study the problem in general relativistic environments, several alterations must be made to the above in order to cope with the physical phenomena that arise, namely length contraction. As we explained in more detail in Part I (Koutsantoniou 2022, Sect. 2.5), the relativistic form of Eq. (11), the GRRTE, is then:

$$\mathcal{I}_\nu(\lambda) = \mathcal{I}_\nu(\lambda_0) e^{-\tau_\nu(\lambda)} - \int_{\lambda_0}^{\lambda} \frac{j_\nu'(\xi)}{\nu'^3} e^{-[\tau_\nu(\lambda) - \tau_\nu(\xi)]} k_\alpha u^\alpha|_\xi d\xi, \quad (15)$$

where $\mathcal{I}_\nu = I_\nu/\nu^3$ is the Lorentz invariant specific intensity, λ the photon affine parameter (Bardeen et al. 1972; Wilkins 1972), $k_\alpha = (k_t, k_\phi, k_r, k_\theta)$ the photon covariant four-momentum and $u^\alpha = (u^t, u^\phi, u^r, u^\theta)$ the contravariant four-velocity of the environment fluid particle. The optical depth is then given by:

$$\tau_\nu(\lambda) = - \int_{\lambda_0}^{\lambda} a_\nu'(\zeta) k_\alpha u^\alpha|_\zeta d\zeta, \quad (16)$$

where all quantities with a prime, such as j_ν' and a_ν' , are measured in the emitting matter's rest frame. From the above equations, one can see that the intensity of the radiation is entwined with the material number density.

In the case where the disk material is very dense and opaque, the radiation is only emitted by a skin layer of the AD. This renders the solution of the GRRTE pointless, if not impossible. This is because the material density, and hence the optical depth, has so steep a gradient that numerical integration is notably challenging. Namely, the steeper the density increment is, the finer the affine parameter partition should be. When this increase is so abrupt, however, the estimated intensity (the lower limit) is far from its actual value. This results in the need of an ever-denser partition mesh that is computationally unattainable. Consequently, another solution must be found, one that includes and accounts for all the relativistic effects brought on by the spacetime grid distortion due to the central mass. A suitable solution was presented in Abramowicz, Ellis, & Lanza (1990) and Miller & Lamb (1996) for central radiation sources. We have also studied this phenomenon much later in Koutsantoniou & Contopoulos (2014) and Koutsantoniou (2022), considering radiation emission from extended noncentral sources, possibly rotating, in Schwarzschild and in Kerr spacetimes.

In these circumstances, the suitable equation to solve in order to derive the received frequency integrated specific intensity I_{rec} ($\text{erg s}^{-1} \text{cm}^{-2} \text{ster}^{-1}$) using the emitted frequency integrated specific intensity I_{em} is:

$$I_{\text{rec}} = \left(\frac{g_{tt,\text{em}}}{g_{tt,\text{rec}}} \right)^2 \left(\frac{1 + \omega_{\text{rec}} k_\phi / k_t}{1 + \omega_{\text{em}} k_\phi / k_t} \right)^4 \frac{1}{\gamma^4 (1 - V^\phi \cos \psi)^4} I_{\text{em}}, \quad (17)$$

where $g_{tt,\text{em}}$ and $g_{tt,\text{rec}}$ are the metric (1) components at the point of emission and reception respectively and $V^\phi = u^\phi / u^t$ the material three-velocity. The first factor of the above product is a result of the time dilation between the point of emission and the point of reception. The second factor is used to take into account the effects brought on by frame dragging. Here, ω_{rec} and ω_{em} are given by Eq. (4) for the reception and emission point respectively. Additionally, k_ϕ and k_t are components of the photon momentum and are conserved quantities

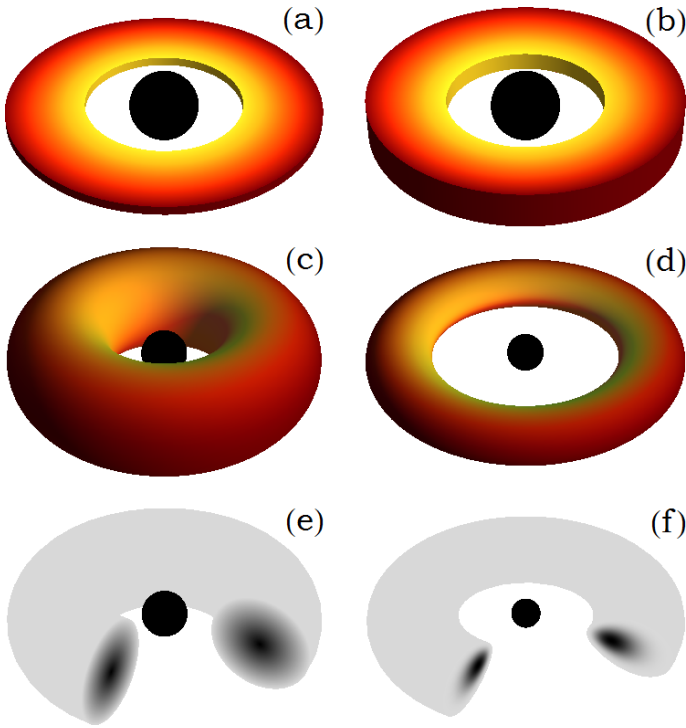


Fig. 3: ADs we present results for. Disks (a) - (d) are optically thick, with temperatures higher for sections closer to the central BH (Sect. 2.3a - d). Disks (e) and (f) are semi-opaque, with higher density toward their material center (Sect. 2.3e - f). Namely, the darker the material color in the cross sections appears, the higher the density in that point is. We can notice that the density increase in (e) is smoother than in (f).

(Bardeen et al. 1972). Finally, the third factor of Eq. (17) introduces the effects of the Doppler shift due to the emitting surface's motion. In this, $V = V^\phi$ is the source circular orbit three-velocity, $\gamma = (1 - V^2)^{-1/2}$ the emitting material Lorentz factor and ψ the angle between the emitting matter velocity and the photon emission direction.

2.3. Accretion disks

In this subsection we review in short the AD models we considered for our calculations. Later on, we discuss and compare the results our computations revealed for these environments, their significance and their implications.

The modeling of ADs is a large area of research with many studies providing a broad spectrum of suggestions. For our work we consulted several recommendations for making the most effective choices. These include Shakura & Sunyaev (1973), Novikov & Thorne (1973), Thorne & Price (1975), Abramowicz et al. (1978, 1988, 1996), Kozłowski et al. (1978), Narayan & Yi (1994, 1995), Esin et al. (1997), Beloborodov (1998, 1999, 2001), Lasota (1999), Igumenshchev et al. (2003), Narayan et al. (2003, 2012), Dubus (2003), Fuerst (2006), Noble et al. (2007), Done et al. (2007), Narayan & McClintock (2008), Sądowski (2009, 2011), Abramowicz & Fragile (2013), Penna et al. (2013).

We consider here six AD models, four of which are fully optically thick and two are semi-opaque. The models we present here are:

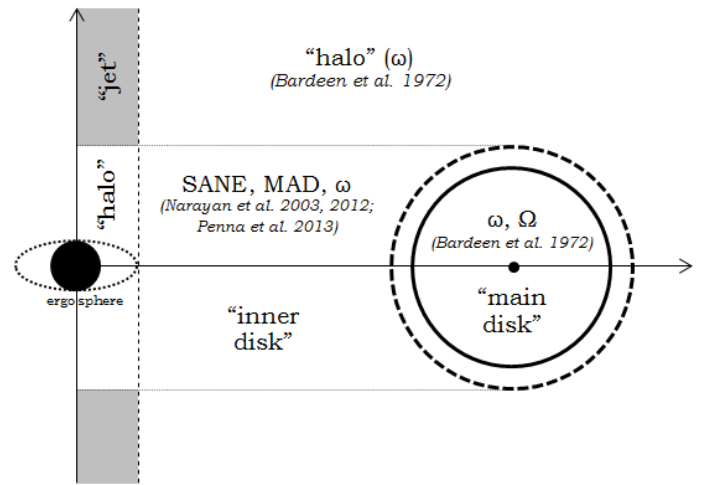


Fig. 4: Miscellaneous velocity regions for the material we considered in the arrangement under examination. The dashed circle represents a thin region near the disk material edge, where matter is slowly escaping or accreting onto the main disk. For this thin transition area, we additionally calculate the field noted by a target moving with velocity a negligible divergence away from the main disk's.

- (a) Slab (toy, snapshot model; opaque): a flat disk of half-height h , with range $r_{\text{ISCO}} \leq r \leq 3r_{\text{ISCO}}$. The cross section is a rectangle (Fig. 3a).
- (b) Wedge (toy, snapshot model; opaque): a sloped disk of inner half-height h , with range $r_{\text{ISCO}} \leq r \leq 3r_{\text{ISCO}}$. The cross section is a isosceles trapezoid (Fig. 3b).
- (c) Torus (toy, snapshot model; opaque): a disk with a circular cross section, with range $r_{\text{ISCO}} \leq r \leq 3r_{\text{ISCO}}$. Cross section center at $(r_c, \theta_c) = (2r_{\text{ISCO}}, \pi/2)$ (Fig. 3c).
- (d) Opaque rotationally supported torus (ORST – self-consistent model; opaque): a stationary and axisymmetric rotationally supported torus with its rotation vector collinear with the BH's (Fig. 3d, details in Koutsantoniou 2022 Sect. 3.1f).
- (e) Semi-opaque LFM torus (toy, snapshot model; quasi-opaque): Semi-opaque version of "Torus". Number density maximized to $n_c = 10^{18} \text{cm}^{-3}$ at the cross section center (Fig. 3e). For this disk we have $a_{\text{abs}} \cdot r_{\text{outer}} \sim 1 - 5$, where a_{abs} the absorption coefficient and r_{outer} the disk's outer radius.
- (f) Semi-opaque radiation pressure supported polish doughnut (PD – self-consistent model; quasi-opaque): stationary and axisymmetric radiation pressure supported polish doughnut (Abramowicz et al. 1978; Kozłowski et al. 1978; Younsi et al. 2012). Maximum number density is $n_c = 10^{18} \text{cm}^{-3}$ at $(r_c, \theta_c) = (12, \pi/2)$. The density gradient increase is much more abrupt for PD than for LFM (we compare Figs. 3e and 3f). For this disk we also have $a_{\text{abs}} \cdot r_{\text{outer}} \sim 1 - 5$.

The above are displayed in Table 1 and more information are available in the online material³.

For the material velocity we looked into assorted studies and decided to split the configuration under examination into various regions with different velocity profiles. We show a schematic of the system sectors in Fig. 4. "Halo" includes observers at rest in the local rest frame, rotating with ω . "Main disk" is the stable, outer AD. The main disk matter can travel in four different ways: at rest in the local rest frame rotating with ω , purely azimuthally

³ Direct link: <https://gitlab.com/leelamichaels/andrt-ii-online-material>

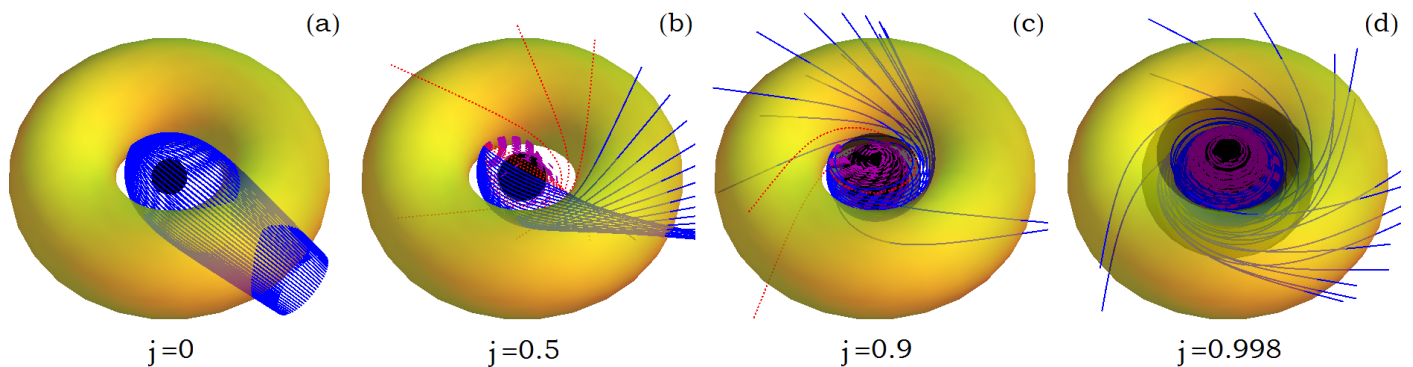


Fig. 5: Output images of the photon bundle edition of Omega for four different values of the dimensionless angular momentum j : 0, 0.5, 0.9 and 0.998, from left to right. We see the BH event horizon (central black sphere), the ergosphere (gray ellipsoid or spindle torus) and the AD (yellow torus). Solid blue lines are trajectories of photons emitted from the AD. Dashed purple lines are trajectories that would originate from the event horizon and dotted red lines are photons that arrive from outside the system. The latter two bring in no additional radiation into the structure.

Table 1: Disk models considered.

Name	Type	Opt. thickness	Cross section
Slab	toy model	opaque	rectangle
Wedge	toy model	opaque	trapezoid
Torus	toy model	opaque	circle
ORST	self-consistent	opaque	droplet-like
LFM	toy model	quasi-opaque	circle
PD	self-consistent	quasi-opaque	droplet-like

with angular velocity Ω (Bardeen et al. 1972), or by slowly infalling, such as in SANE and MAD (Narayan et al. 2003, 2012; Penna et al. 2013). “Inner disk” includes the region of infalling material and thus contains only matter at rest in the local rest frame and infalling material mimicking SANE and MAD. The “jet” region is a section of a cylinder centered at the setup’s rotation axis that includes the BH’s ergosphere and thus has a radius $r = 2M$. This region is only assumed to exist above a certain adjustable height, further away from the BH. In that volume of space, we can have matter at rest in the local rest frame and matter flowing outward with a certain adjustable velocity. We may also consider subregions there moving differently. For example, we can assume a narrower cone or cylinder with radius $r = M$ with stronger outflow and faster velocity or even with velocity of the opposite direction (see e.g., Asada et al. 2016; Nakamura et al. 2018; Park et al. 2019).

3. Results

In this section we show our results with pictures, density plots and histograms. These include photon trajectories, radiation force magnitudes, AD images, BH spin estimations and radiation degenerated massive particle orbits. This material was created while studying assorted setups of disk models, spin parameters, velocity profiles, and more.

In each of the subsections we describe the results attained by the respective code and discuss their possible implications. Moreover, at the end of each part we briefly describe the potential improvements, extensions, and applications for the program in relative subjects.

3.1. Omega results: bundles of photons

Omega is the heart of most of our codes. It solves the differential equations of motion and studies massless and massive particle trajectories. Extensive work on particle orbits in BH environments and strong gravity can be found for example in Levin & Perez-Giz (2008), Levin & Grossman (2009) and the following works.

Since the latest version of Omega is not graphical, we show here the results of an earlier version designed and used to show photon bundle trajectories. In Fig. 5 we see photon orbits reaching the same target-observer situated on the AD. Namely, moving backward, we trace the trajectory of a photon possibly received in a specific direction. If this path crosses the AD at any point, then it carries along radiation and energy. Under different circumstances, a photon would not reach the target carrying energy, since it would have to be emitted from the BH event horizon or from somewhere outside the system.

One of the study facets this code can be directly used for is the examination of particle trajectories and how these are affected by spacetime rotation. For example, in Fig. 6 we see the effects of increasing BH spin on photons launched in different angles and moving in the equatorial plane. Moving to higher spins, we see that, as expected, the photons reaching the target move along with the spacetime rotation itself (clockwise). The sky scanning process and the spacetime rotation effects on photon trajectories can also be seen in a video found in the link mentioned in the following subsection.

Before continuing on, we describe our thoughts about the possible extensions for this program. Numerous further studies can be made using the aforementioned code. For example, Omega can be extended to study particle trajectories in X-ray binary systems, light rays in multiple-star, and more. Additionally, the capability of following photon trajectories in proximity to massive or compact stellar objects can be used to examine and analyze phenomena related and influenced by gravitational lensing (Refsdal 1964; Blandford & Narayan 1992; Narayan & Bartelmann 1996; Bozza 2010).

3.2. Infinity results: disk images and radiation forces

In order to study the radiation forces appearing in various points of the disk models described in Sect. 2.3 we have developed the code Infinity. Using this setup, we have run a large number of

Table 2: Infinity code executions for the various disk models and spin parameters.

BH spin	Disk model					
	slab	wedge	torus	ORST	LFM	PD
0	168	170	163	184	496	454
0.5	182	177	176	188	478	484
0.9	156	158	148	179	424	488
0.998	-	-	-	191	414	488
Sums	506	505	487	742	1812	1914
Total number of runs: 5966						

Notes. The first four models are the opaque disks we described earlier. The slab is discussed in Sect. 2.3a, wedge in 2.3b, torus in 2.3c, and ORST in 2.3d. The remaining columns are the two semi-opaque disks we mentioned in Sect. 2.3. We can find LFM in 2.3e and PD in 2.3f. (Any of the results can be made available upon request.)

executions for all the models considered and in assorted BH spin parameters. The amount of executions for each of these environments can be seen in Table 2. These executions are for assorted target locations in each of the systems. These can be in the configuration’s interior ($r < r_{inner}$) or exterior sectors ($r > r_{outer}$), on the surface of the AD or away from it, inside the system outflow regions or scattered in the halo. Observers are thus spread throughout the entire volume of the configurations and record the incoming radiation and the respective force. Each of these execution targets can be seen as colored dots or triangles in Figs. 8 and 9 and Figs. 2-7 of the online material. More information on the selected AD characteristics can also be found in the online material.

In Fig. 7, we see some Mollweide projection sky maps of the incoming radiation for the models mentioned in Table 2. In addition, videos of flights around and if possible through the disk for all the models we studied, can be found on youtube.com, under the name of this work’s creator "Leela Elpida Koutsantoniou" ⁴.

Further on, in Figs. 8 and 9, we show result images for the radiation force magnitude and distribution for two of the ADs considered for spin $a = 0$. In addition, in the online database, we show multiple large images in assorted a that demonstrate the radiation four-force components for the previously mentioned ADs for various spin parameters.

We note that in the aforementioned figures, we use red filled “up” arrows to mark positive and blue or green empty “down” arrows to mark negative radiation four-force components. These marks act in the same manner as the diffuse colors and assist in the easier distinction of force signs in areas where radiation forces approach zero and hence plot colors approach white. Furthermore, black empty circles represent a force value exactly equal to zero and gray dots represent a null force value due to disk model or spacetime restrictions (e.g., static limit). We finally note that each of these marks represents the results of one full code execution run. In some of the results appearing in these images, we have applied an enhancement process (see Koutsantoniou 2022, Sect. 4.2) to increase the resolution by twenty-five times. We note, however, that it is also possible to change that to a higher or smaller number, or to remove it completely. It is additionally possible to run more than one application of the process.

Continuing on, we examine Figs. 8 and 9 in detail. In Fig. 8 we have a semi-opaque LFM disk and in Fig. 9 an opaque ORST disk. These density plots show the sign and magnitude of the BL

four-force components in dyn ($1 \text{ dyn} = 1 \text{ g} \cdot \text{cm/s}^2 = 10^{-5} \text{ N}$) at several points outside, near, and if possible inside some of the disk models mentioned in Table 2 and Fig. 7. Each line of these pictures refers to target particles belonging to one of the aforementioned velocity groups: “halo” includes particles moving only with ω due to the spacetime rotation (Eq. 4), “disk” includes particles in circular orbits with speed Ω (Eq. 10), “SANE” and “MAD” refer to particles in inspiral orbits, mimicking these two accretion situations and “jet” refers to target particles that also have a radial outflow velocity component pointing outward.

The first four lines of each picture are typical poloidal plots: the horizontal axis measures the cylindrical distance ϖ from the central axis and the vertical measures the height z from the equatorial plane, which is also a symmetry plane for the ADs. The fifth line shows plots rotated 90 degrees: the horizontal axis is z and measures the height from the equatorial plane and the vertical axis is ϖ , measuring the cylindrical distance from the system rotation axis. The columns in each plot group show in order the distribution of the t -, ϕ -, r - and θ - force components.

The various disk model results differ decisively from each other and we thus use different colors for easier identification. In each color scheme chosen, seen to the right of the corresponding plot, the lower half represents negative (blue, green) and the upper half, positive force values (magenta, orange). In all the schemes, white color is in the middle and stands for zero force components.

Some of the results presented in Figs. 8 and 9, as well as the online database material are expected, while others are not. Moreover, we mark that the deviation of the BL halo f^t plot from zero gives us an estimation of the numerical and computational errors present in our calculations. These estimated errors appear to be adequately below the forces we are attempting to calculate, so they are well within acceptable limits.

Looking at the first column of a picture group, we can see the effects of the radiation on the energy absorption amount and rate by the target particles. The images provided by the simulations are in qualitative agreement with the expected results. For instance, we can see the energy transfer getting stronger, the closer we get to the central object. In that region the absorbing and emitting particles of the material rotate and move faster in their trajectory. This means that the radiation is further beamed along the motion direction. In addition, since at these points we are outside the AD, the incoming radiation is getting further and further away from uniformity. These two aforementioned arguments explain why we expect there the PR effect to be more potent and to display its braking impact stronger than in other areas.

On the contrary, when examining areas further outside the disk, the radiation is closer to uniformity. Thus, the PR effects are more easily concealed by the uniform and beamed radiation emitted by the moving material along its direction of motion. Additionally, we note that the farther away we move from the BH, the less curved spacetime is and, therefore, the less arced the photon trajectories get. In total, we hence note the appearance of strong braking forces $f^t < 0$ for areas with $\varpi \lesssim r_{inner}$ and closer to the rotating z -axis, where r_{inner} the inner edge of the disk. Respectively, for increasing cylindrical distance from the rotation and symmetry axis $\varpi \gtrsim r_{inner}$, the force turns positive, $f^t > 0$, but with notably smaller magnitude. We also note that for semi-opaque ADs these observations continue to stand, but the zero force surfaces move somewhat toward the configuration exterior. This is anticipated, since adequate values for the optical depth are expected to accumulate for the photon trajectories in order to set in motion the processes described above.

⁴ Direct link: https://www.youtube.com/playlist?list=PLlIB2cSVqLeu6urpQ9u5Gk8LsA_00UxRj

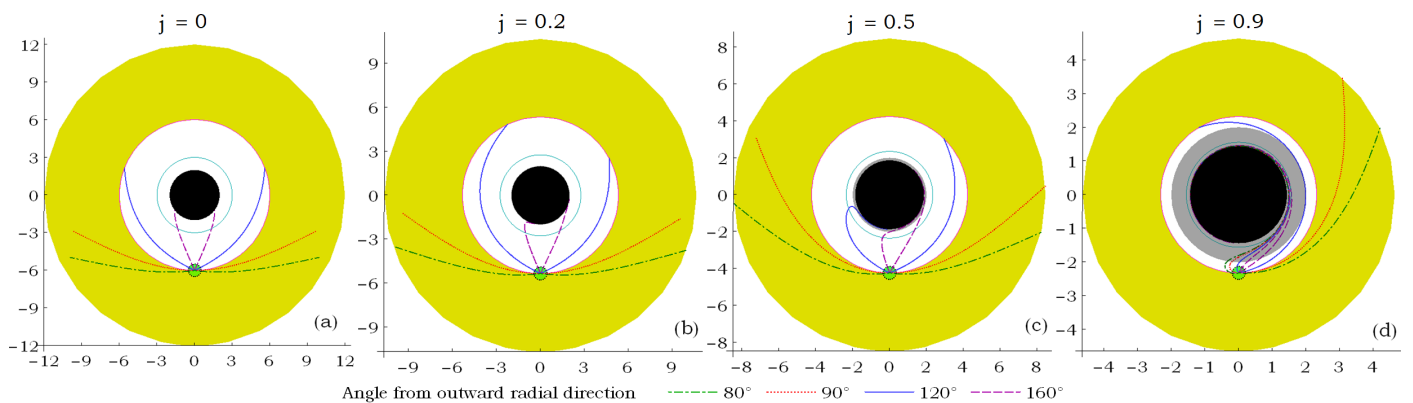


Fig. 6: Equatorial photon trajectories launched from the AD material orbiting a clockwise rotating BH with increasing dimensionless angular momentum j (from left to right). We see the event horizon (central black disk), the ergosphere (gray annulus), the photon ring (solid line cyan inner circle) and the AD (outer thick yellow annulus) from $r_{\text{inner}} = r_{\text{ISCO}}$ to $r_{\text{outer}} = 2 r_{\text{ISCO}}$. The photons are launched at angles from the outward radial direction: 80° (dot-dashed green), 90° (dotted red), 120° (solid blue), 160° (dashed purple). We notice that as the BH spin increases, the photon trajectories reaching the observer at the bottom (green disk) get dragged along by the spacetime rotation.

The second column shows the azimuthal component of the radiation force. The ϕ -component of the radiation force f^ϕ follows the profile and distribution of the f^t force in the vast majority of cases. This means that in the inner regions of the arrangements, in cylindrical radii $\varpi \lesssim r_{\text{inner}}$ the force is negative, $f^\phi < 0$, viz. braking. On the contrary, further outward for $\varpi \gtrsim r_{\text{inner}}$, the azimuthal radiation force turns positive, $f^\phi > 0$. Continuing further out and departing the setup, we record the expected decrease of radiation force magnitude and its eventual extinction. For opaque disk models we also note the presence of an additional area (Fig. 10). This area can perhaps be described as a "shadow" of the AD. Namely, for observers in regions outside the AD and at small heights from the equatorial plane, the azimuthal radiation force turns negative again. This happens because these areas are partially shielded from the bulk of the radiation emitted from the inner and hotter regions, due to the opaqueness of the intervening material. This leads to the total received radiation magnitude being notably reduced. This alteration, in conjunction with the strong anisotropy of the observed radiation source, makes the PR effects more prominent and eventually dominant. We hence note the existence of a region displaying again braking forces in the direction of the disk rotation.

The third column shows the radial four-force component f^r recorded for each disk model and it is also in qualitative agreement with the expected results. When the target is further out from the disk, it receives more radiation coming from its interior local sky hemisphere than from its exterior one, and is thus pushed further outward. For a target further inward from the disk, the opposite occurs: the outer hemisphere receives more radiation than the inner one, and the particle is pushed toward the BH.

The fourth column shows the θ -force f^θ in the poloidal plane and its effects on the structure particles. We mark that the poloidal angle θ is measured the typical way: $\theta = 0$ for points on the positive z axis, $\theta = \pi/2$ for the equatorial (x - y) plane and $\theta = \pi$ for the negative z axis. We first notice that, as expected due to symmetry, this force disappears in the equatorial plane. Additionally, we find it becomes negligible the closer we get to the vertical rotation axis. In almost all the cases this force is negative, which means it pushes the material upward toward the ro-

tation axis. In the very few cases where the force sign is positive, we note that these points are in small heights and in very close proximity to the ergosphere or the event horizon. At these points, the targets can only see a small part of the AD in the sky around them. As a consequence, the received radiation at these points is governed by the Einstein - Khvolson "echo" ring of the opposite side of the disk, across the BH. The targets there are thus pushed toward the equatorial plane in contrast to the majority of cases. Respectively, when we examine the bottom half of these configurations (i.e., for $z < 0$), we notice the expected opposite behavior. The θ -force there is almost everywhere positive, pushing material toward the Oz' axis. Apart from these points, there is also a very limited quantity of points that record $f^\theta < 0$ governed by the Einstein - Khvolson echo ring, as explained before.

We continue on to investigate the radiation forces documented in the central outflow regions of the systems. In these regions, a directed outflow or a jet could be formed, moving outward and away from the compact object, the AD and the highly curved spacetime. For target particles moving in these areas, we assume two velocity profiles or more. We hence study the radiation repercussions on material moving in the underlying spacetime grid and possibly outward. Before reviewing the results, we must keep in mind that the radiation source is the AD and is situated behind the target particles as they move outward. Keeping this fact in mind, the results are qualitatively expected. In the radial direction, the source of light is inward, behind the target particles and is thus driving them outward ($f^r > 0$). For the poloidal direction, the emitting material is located below the targets and is consequently pushing the material toward the rotation axis ($f^\theta < 0$). As for the other directions, t and ϕ , we again see that they are consistent with each other and appear negative ($f^t < 0$, $f^\phi < 0$). This is also expected if we consider the nature and setup of the forces. Namely, for the azimuthal direction of motion the emitted radiation, the light source is highly anisotropic and the bulk of radiation is detected in angles in the vicinity of 90 degrees. This entails and explains the increased prominence of the PR braking effects.

We should note here, however, that the investigation is perhaps significantly dissimilar if we examine a slightly different environment. This similar yet different environment is a more realistic outflow region of a BH. That is to say that, we will per-

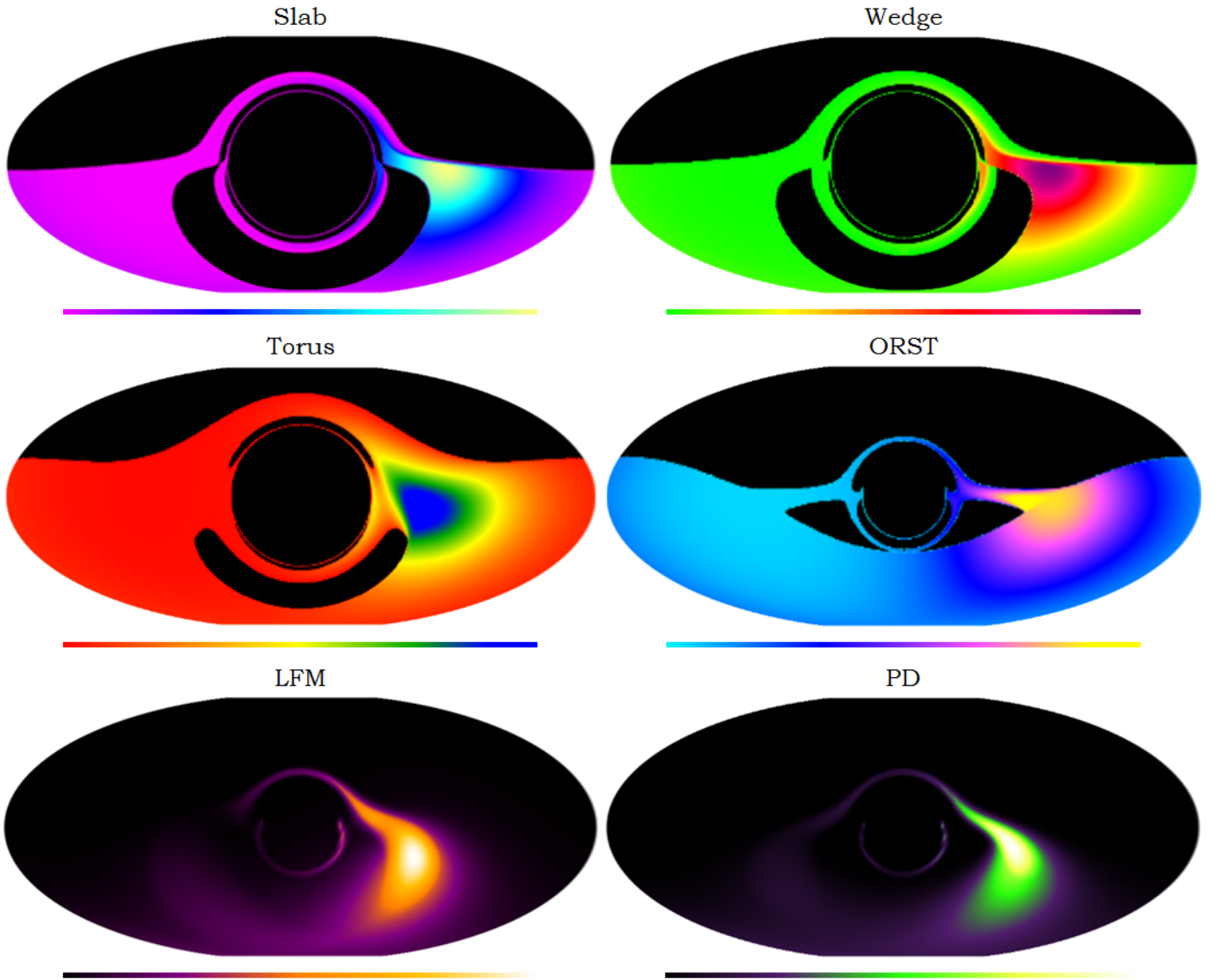


Fig. 7: Mollweide projection sky maps of the frequency integrated specific intensity I . Each image shows the run results for a different disk model (Sect. 2.3a-f). Below each image, the model's color scale is displayed from minimum (*left*) to maximum (*right*). The circle of radiation in the center of each image is an Einstein, Khvolson or "echo" ring (Sauer 2008) created by photons traversing the disk area and reaching the observer after traveling above and below the BH horizon and AD. The radiation intensity difference between the left and right half of each image is due to the rotation of the AD. Radiation from material moving toward the observer is boosted, while radiation from material moving away is deboosted.

haps obtain different results if we look into forces on material in an outflow that is not empty but contains blobs of matter. The radiation force profiles there, are shifted and altered due to the existence of hot, emitting, and moving material before, after or adjacent to the receiving target. Such an examination requires an attentive look and should be looked into meticulously in a future study.

The force density plots (Figs. 8, 9, and respective online material) are useful for many reasons. First of all they show us the magnitude and the sign of the radiation forces created by each disk model setup. They also reveal the differences between the models considered and their diversity. Furthermore, they provide us with novel and valuable information about the geometry and structure of the radiation field created in such objects. We can therefore see, for example, in which portions of the AD the forces are stronger or smoother. We can additionally notice the rearrangement of zero force surfaces (whiter shades of colors

in the plots) for the assorted disk models and its displacement for increasing values of the BH spin parameter. We can also see which specific force components have effects that influence and modify the stability and the evolution of the disk. We can investigate, for instance, whether the radiation has an impact and if it can modify the rotation of the AD material itself.

In addition to the aforementioned figures, we can examine the histograms comparing the radiation force components for the various models we studied. For example we can survey Fig. 11, as well as the online material and see which setups record stronger forces. We can hence examine the significance of the assorted disk characteristics and consider their results. We can consequently ponder on the importance of the disk volume versus its optical thickness, its vertical height, its rotation speed, its distance from the central compact object, and many more.

If we examine the force density plots and the comparative bar plots for all the disk models and spins considered, we can

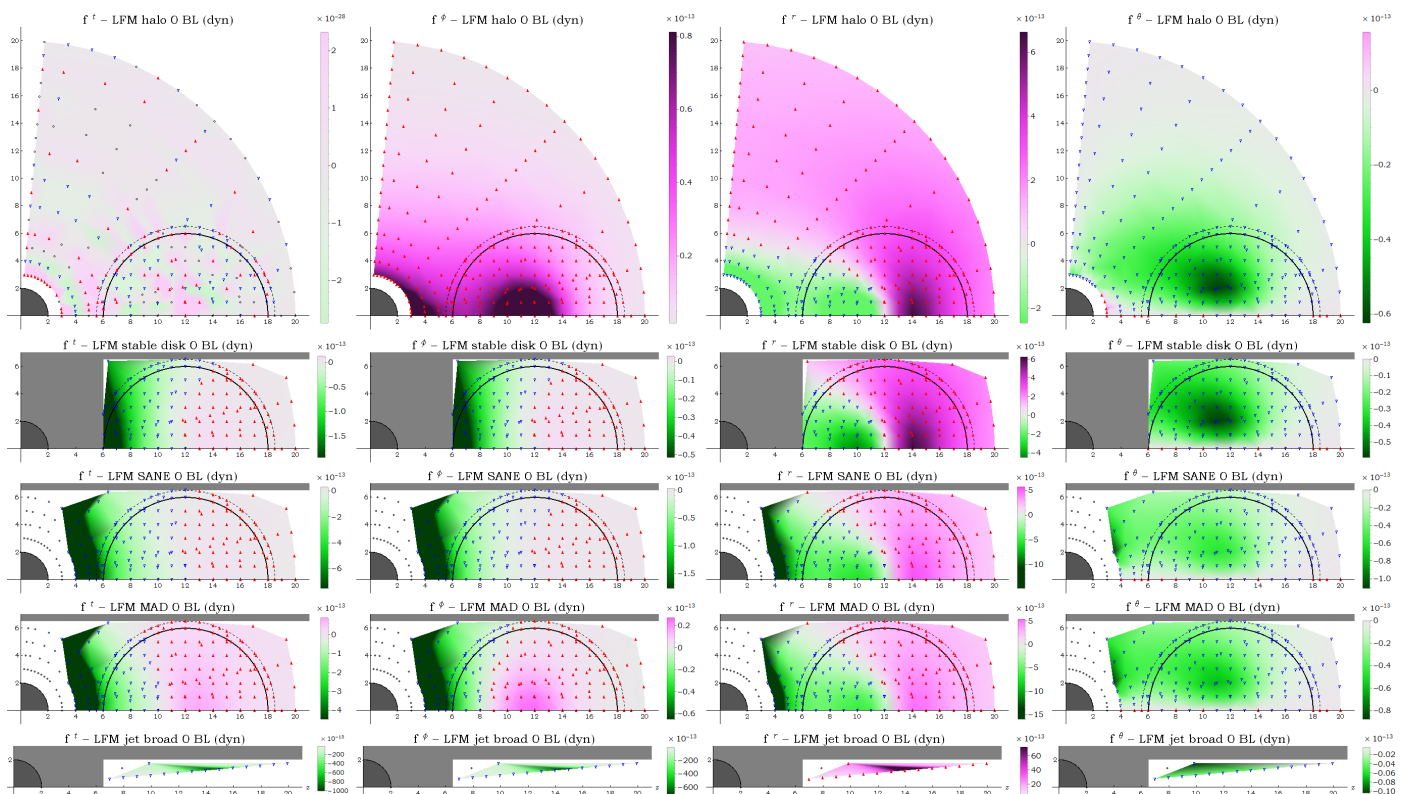


Fig. 8: Forces in dyn for the LFM semi-opaque disk model (Sect. 2.3e) for BH spin $a = 0$ in BL coordinates. All axes use geometrical units and the numbers shown are in M . The *first line* of plots (axes x - z) shows the radiation forces exerted on electrons at rest in the local rest frame (Eq. 4). The *second line* (axes x - z), forces on electrons moving with angular velocity Ω (Eq. 10) in the appropriate spacetime region. The *third and fourth line* (axes x - z) show radiation forces exerted on electrons moving with velocity profiles mimicking the SANE and MAD models material motion. The *fifth line* (axes z - x) records radiation forces in an outflow region. The material there, a certain (adjustable) distance away from the horizon, has additionally a velocity component pushing it outward along the z axis, as it would be moving in the outflow region of such systems. More spins and environments can be found in the online material.

draw some conclusions about the recorded radiation. The Torus model, a voluminous and borderline opaque AD appears to generate and exert the strongest radiative forces throughout its entire arrangement onto all the disk or free material. Then follows the Wedge model, which is also opaque but with a much smaller vertical height and smaller radiative forces. Following closely, we have the opaque Slab model that is similar to Wedge but with a constant vertical height through its structure. These two models have characteristics and observed radiation effects very close to each other and often intermixing. We note, however, that in total Wedge records slightly higher radiation forces. We mark here, that this pair of models offers a unique opportunity to examine the radiation effects onto the perhaps puzzling polar radiation forces and the diverse effects onto material close to the rotation axis and the outflow region.

The next in force magnitude model is the opaque ORST, a model that significantly changes its size for increasing BH spin. Nevertheless, the disk's cross section center region only changes slightly and moves outward for increasing spin a . Additionally, we observe in the bar plots that the geometrical characteristics of this model have in some cases interesting and unexpected consequences on the radiation forces exerted on the material (e.g., for $a = 0.9M$).

After that, we have the semi-opaque disk models that demonstrate the production of softer radiation fields and follow the opaque disks in force magnitude. We first encounter the polish

doughnut semi-opaque model PD. We notice that a setup of this kind appears to generate stronger forces in the outflow regions of the system, compared to most of the other models. This is a subject well worth a more attentive look, since it has important repercussions on the flow of mass and energy along the rotation axis. The effects of the radiation field should thus be reviewed about their possible ramifications and influence on the outflow and the jet, and more importantly on its collimation.

Along with the polish doughnut PD, we have the semi-opaque LFM disk, which also creates a soft, but different radiation field. This disk model has precisely the same geometrical attributes as Torus but is instead quasi-opaque. Comparing these two models, we can draw useful conclusions about the impact of the disk opacity and stratification. Namely, even though the two light sources are of the same extent, the LFM disk exhibits a far weaker radiation field. We can thus experiment with the density gradient of the disk model and measure the consequences on the radiation field and the forces exerted. Moreover, by comparing the LFM disk with the PD, we notice again that even though LFM occupies a larger volume of space, the PD records larger radiation forces exerted on the material. These two points thus complement each other and agree with the aforesaid radiation notes. Most importantly though, they hint that the primary factor responsible for the forces recorded is not the AD volume, but the material density increase rate instead.

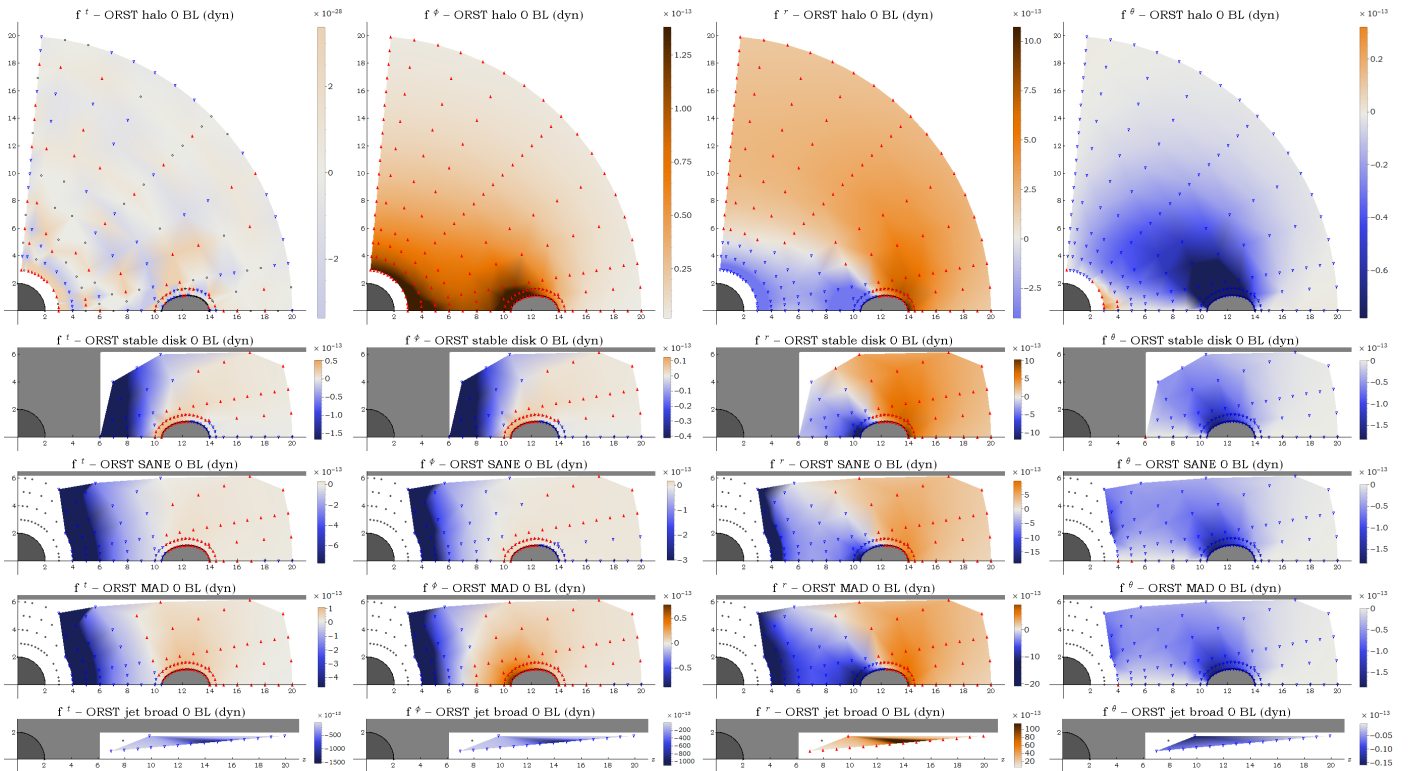


Fig. 9: Forces in dyn for the ORST disk model (Sect. 2.3d) for BH spin $a = 0$ in BL coordinates. All axes use geometrical units and the numbers shown are in M . Plots shown in the same manner as described for Fig. 8. More spins and environments can be found in the online material.

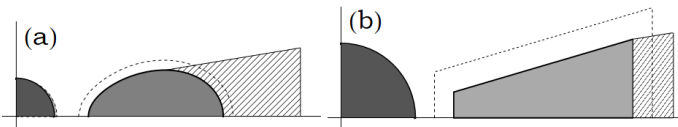


Fig. 10: AD "shadows". Partially shielded regions (in *stripes*) of the system next to opaque ADs. The disk opacity obscures emitting regions of the material reducing the recorded radiation and thus unveiling the PR drag contribution.

Some other important notes for all the above figures are also the following. First of all, even though the forces may seem small or negligible, we should always keep in mind that these forces $\sim 10^{-13}$ dyn act upon the electrons and therefore a mass $\sim 10^{-27}$ g. This means that the (classical) acceleration due to radiation is $\sim 10^{14}$ cm/s² and it is primarily acting upon the material electrons since $f_e/f_p \sim (m_p/m_e)^2$. This causes the material electrons to gradually brake, losing energy, or accelerate, gaining energy. This then results in electrons inspiraling further in toward the central object or being slung outward. The electrons' displacement then induces a charge separation between the material components. This then forces the protons (or ions) to follow the electrons into lower or larger orbits, subsequently causing parts of the AD material to slowly infall into the central BH or move outward.

We remark here that the process of electrons changing rotation angular velocity and radius mentioned above, also leads to the generation of a ring electric current within the AD material. This current's central areas are situated near the disk's inner and outer edges. This hence results in steady generation and accumulation of poloidal magnetic field loops in the setup.

Depending on the material's physical properties, principally its magnetic Prandtl number Pr_m ⁵, some parts of this material bring one polarity of these loops toward the center as they infall, while the opposite loop polarity is carried outward. Taking additionally into consideration the differential rotation of the AD, these magnetic field loops get twisted and then open up, filling the system with smaller magnetic loops and lines as described in Contopoulos et al. 2006, 2015. This magnetic field formation, evolution and possibly reconnection is a very intriguing subject that is well worth of thorough research and attentive investigation in a separate and specifically focused study.

Finally, looking closely at the density plots, one can notice that the t -force zero curves are not located at the same places as the ϕ -, r - and θ -force zero curves. This was not an anticipated event and it is worth mentioning explicitly since it gives rise to perhaps unexpected three-force components close to and through the disk.

In conclusion, we can consider the interesting possible extensions and usages of the Infinity code. We can further investigate the radiation and energy exchanges between various members of more complex arrangements. For instance, we can inspect the assorted transactions between partners of multiple-star systems including main sequence stars, giants, or supergiants. These configurations may or may not contain ADs as well. Further on, the algorithm can be used to take an attentive look into the electrical and consequently magnetic effects occurring in the systems. Namely, our results revealed the generation of ring currents throughout the disk material due to the forces accelerating or braking the electron population. These developments thus

⁵ The magnetic Prandtl number Pr_m (dimensionless quantity) is the ratio of momentum diffusivity or viscosity to magnetic diffusivity.

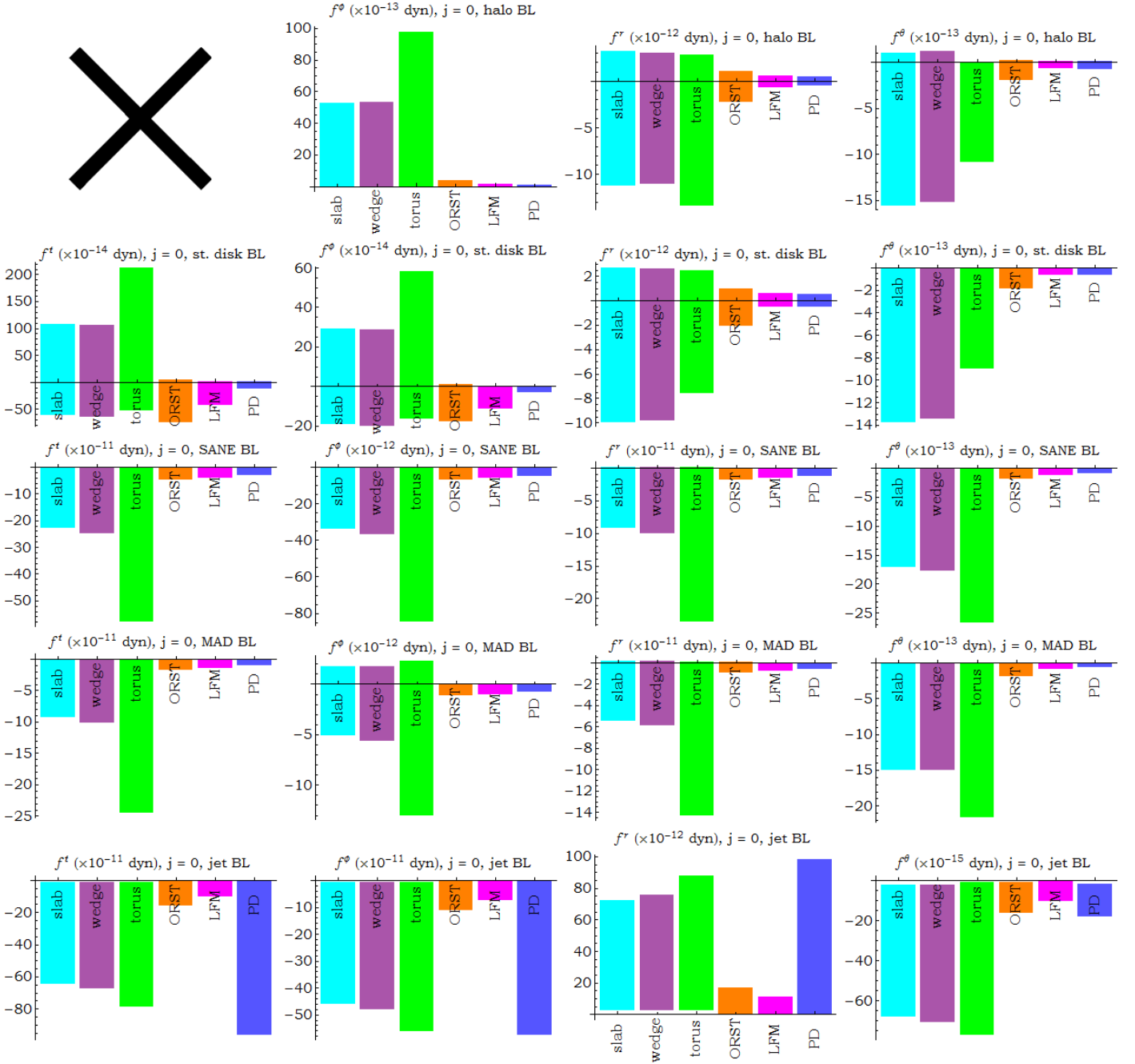


Fig. 11: Comparison of the radiation force components for the various AD models studied in $j = 0$ spacetime. The models are described in Sect. 2.3 and are shown in the plots in the same order. The halo t -force comparison (*top left*) is not displayed since it only provides computational error information. More spins and environments can be found in the online material.

lead to the generation of poloidal magnetic fields. The magnetic field lines in the structures later on extend, curl, twist, and open up, filling the volume of space inside and possibly at areas further out the configurations. These areas are thus filled with magnetic loops of the opposite curl. Keeping in mind the gradual extension of these opposite curl magnetic loops, further investigation can be conducted into the possibility and repercussions of magnetic reconnection. In addition to the above, the particle trajectories and equilibria should be reconsidered, taking into account the new radiation and magnetic field environment conditions (see for example [Bini, de Felice, & Geralico 2011a](#)).

(High resolution images of all the plots can be found in the electronic form and the online material of this work.)

3.3. Elysium results: AD & BH photographs from infinity

Elysium was created in order to construct BH and AD system images as they would be observed from further away from the disk, or from "infinity". Similar work from different perspectives was also presented for instance in [Broderick & Loeb \(2005\)](#), [Mościbrodzka et al. \(2014\)](#), [Davelaar et al. \(2018\)](#), [Event Horizon Telescope Collaboration \(2019b\)](#) and subsequent works.

For our work, we have run several high resolution executions that show various AD models with different sizes, shapes, temperature profiles, and spins. Furthermore, many other such models and environments could be studied using Elysium, such as Novikov-Thorne ADs ([Novikov & Thorne 1973](#)).

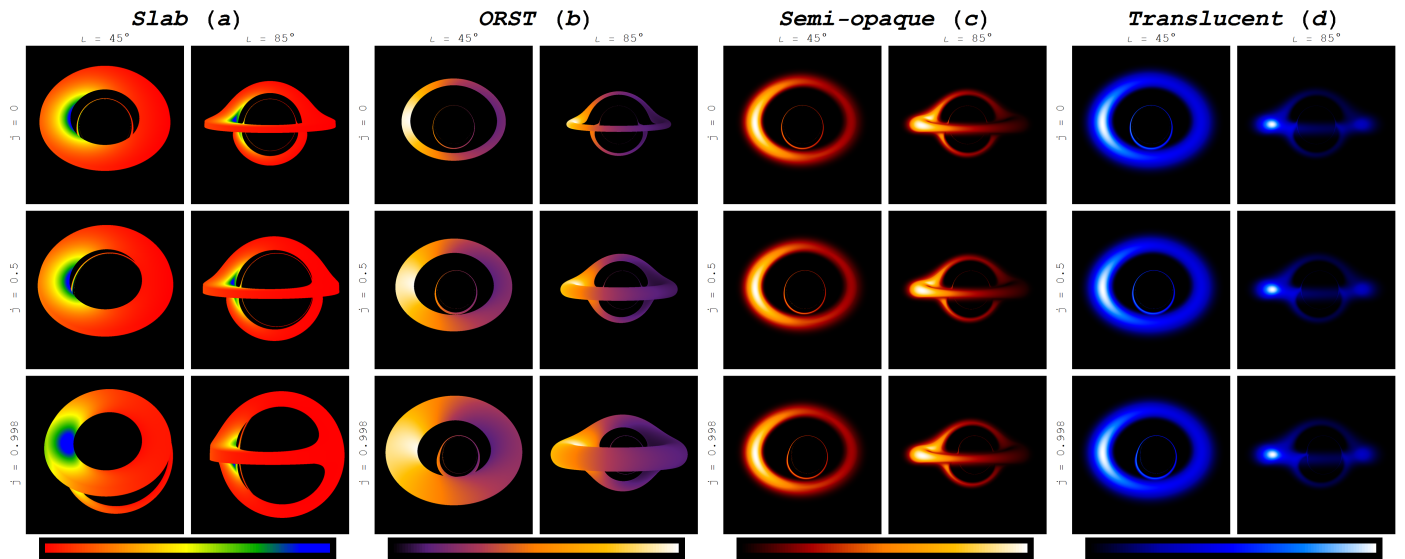


Fig. 12: Frequency-integrated specific intensity taken by running *Elysium*, from left to right, for the opaque slab (Sect. 2.3a) and ORST (Sect. 2.3d), the semi-opaque and the translucent polish doughnut (Sect. 2.3f). In the left column of each set of pictures, there are photographs taken from a screen with 45° and in the right, with 85° inclination. Each line has a different BH angular momentum. Moving from top to bottom these are $j = 0$, $j = 0.5$ and $j = 0.998$. Below each picture group, we can see the used color scheme from minimum to maximum. The produced images are in agreement with other works, e.g., [Younsi, Wu, & Fuerst 2012](#).

Here, we show result images for different tori models of assorted spins and inclinations: in Fig. 12 we see a slab disk in (a), an opaque rotationally supported torus (ORST) in (b), a semi-opaque polish doughnut in (c), and a very low absorption, translucent polish doughnut in (d).

We note here that black pixels in the aforementioned images do not necessarily signify the absence of material. This is due to the fact that even in real observations, very low density of material cannot be photographed. A typical example of such cases is the disk outer layers, as can be seen in Figs. 12c and 12d. To make this more apparent and to give a better idea of the actual AD volume, we show in Fig. 13 the photograph picture of the same AD in more natural colors (left) and in pseudocolor (right). In addition, we can notice observationally expected phenomena, such as limb darkening in Fig. 12c.

The application of this program is useful because, apart from simpler figures, it allows us to create the expected images produced by a multitude of observations. For example, we may have images created by combining high energy (e.g., X-rays) observations with lower energy (e.g., optical, radio) observations (see e.g., Fig. 14). We can thus create images of objects with varying amounts of different components, such as dust grains, molecules, dense free electrons, magnetic fields etc.

Subsequently, we consider the feasible expansions of the *Elysium* code. In combination with the aforementioned extensions of the *Omega* routine, we can additionally enhance *Elysium* in order to carefully look into evidence of gravitational lensing. Specifically, in addition to imaging disks around massive compact objects, we can add other systems, stars or galaxies in the background, behind the compact object and survey the gravitational lensing evidence and data. Another avenue of investigation can be noticed if we closely look into Fig. 12. There, we can notice that the primary Einstein - Khvolson echo ring does not have a constant size, but rather depends on the distance of the disk from the event horizon. For instance, we notice the first echo ring of the leftmost disk to be larger than the rest and, in cases, larger in size than the disk itself. This is because the

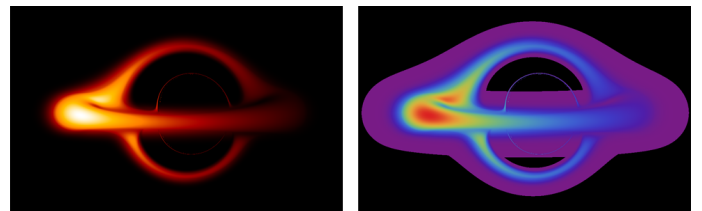


Fig. 13: Photograph picture of the same semi-opaque polish doughnut (Sect. 2.3f) shown in natural colors (left) and in pseudocolor (right). On the right, low density material is shown in purple instead of black, revealing the actual volume of the AD, which is significantly larger than what appears in more natural colors on the left.

inner edge of this disk model is further inward than in the other cases. This could perhaps be of use in certain cases, viz. in cases where the main disk is too small, too close to the event horizon, or partially concealed by intervening material. In such cases, detection of the first Einstein - Khvolson echo can reveal evidence about the disk material and its distance from the central object, even though the main disk is not visible or discernible.

3.4. Tranquillity results: BH spin estimation

Tranquillity is used to simulate and study images of disks rotating around a central object. The code examines images of arrangements at infinity and gives an estimation of the disk inclination relative to the line of sight and the central BH spin. Processing of a multitude of execution results leads then to the generation of divergence plots that can be used as a scale in order to promptly appraise the BH spin of a configuration.

In Fig. 15, we can see two divergence results plots given by the execution of 240 high resolution runs of *Tranquillity*. The ADs under study there, are of varying inclinations, ranging from 0° (face-on) up to 90° (edge-on). In order to create these composite plots, the code was run for inclination angles every 5° ,

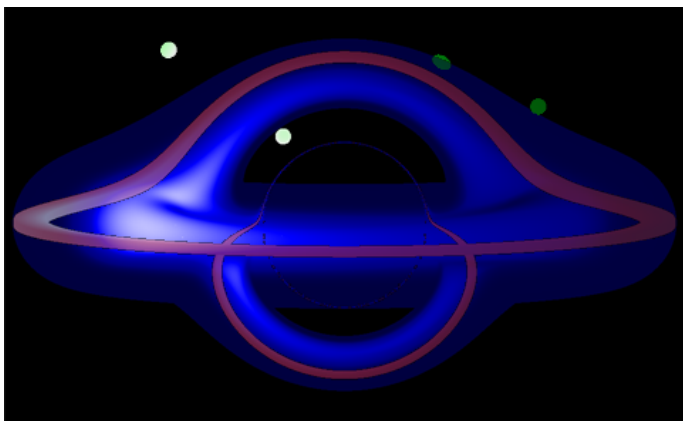


Fig. 14: Photograph picture of an AD in multiple wavelengths. The inner regions (electrons) are observed in X-rays (*blue*) and the outer, obscured, and colder regions (gas, dust, molecules) in infrared (*red*). There is also material of medium temperature above the disk observable in optical wavelengths (*green*).

plus runs for an angle of 89° . We show here the study results of two very different tori. In the top plot, the AD changes significantly in size, inner and outer radius and vertical height for each BH spin. On the contrary, in the bottom plot the torus size, shape and location remains approximately the same for all spins. For both cases, there is a clearly visible trend for the divergence evolution of the same BH spin across the various inclinations.

Tranquillity shows good quality of results for the inclination estimation (see Koutsantoniou 2022, Sect. 4.4). We can thus use this attribute along with the aforementioned divergence plots in order to have an assessment for the central BH spin parameter. Results of such randomized tests can be seen in Table 3. There, we have a comparison between the actual AD inclination relative to the line of sight and the estimated disk inclination given by the code. Moreover, we have the comparison between the true BH spin parameter and the spin derived by the code. These two quantities appear to be in adequate proximity and the relative spin errors are limited and acceptable.

Further on, we consider the improvements that could be made to the Tranquillity code. We should remember that the results of this algorithm are affected by the AD model and its inner edge, but certainly do not rely on this convoluted and puzzling piece of information. In theory, this algorithm investigates how obtainable observational data can be used to provide an estimation of the central object spin, whatever that object might be. This means that, the better and clearer the observational data are, the better the spin estimation is. The first step toward a better program is the creation of a larger information database. This will allow the code to automatically compare the observational input to a broad spectrum of statistics and discern the best fit and divergence scale plots for the disk observed. However, for such a complex and extensive undertaking, significant amounts of testing are required. In addition, cases with particular disk or spacetime geometrical situations should be recognizable and dealt with by the program automatically.

3.5. Burning Arrow results: orbits degeneration due to radiation

Burning Arrow was created in order to study the effects of the disk's radiation onto the orbiting particles' motion itself. Ignoring radiation, matter in the AD rotates around the central object

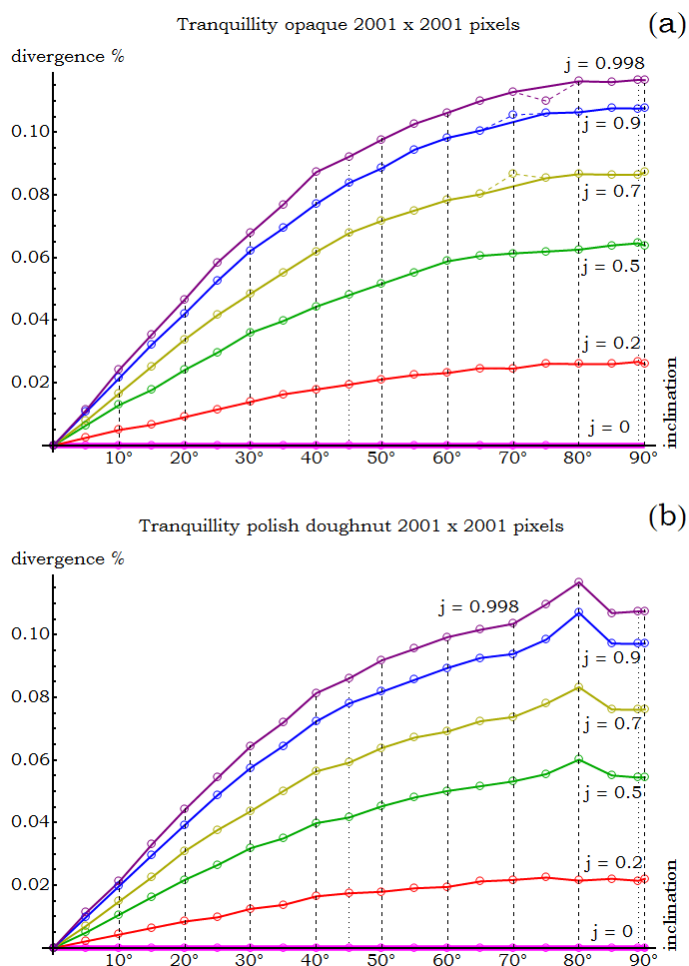


Fig. 15: Tranquillity code collective results, where the circles represent execution results. The AD (a) on the top (Sect. 2.3d) changes significantly across various spins, while the AD (b) on the bottom (Sect. 2.3f) remains practically unchanged. There is a clear trend for the divergence evolution for every BH spin. In these plots, we also include the three worst code results, depicting them with the dashed colored lines.

in a fashion similar to the circular orbits presented in Bardeen et al. (1972), or relevant variations, such as SANE and MAD.

Burning Arrow reads and uses data from Infinity results about the radiation forces at various points in the system. It then calculates the acceleration components brought on by the disk's radiation. Finally, it determines and plots the consequent particle trajectory for assorted velocity profiles. This final particle trajectory now includes the additional radiation effects.

We show in Fig. 16, some of our results for a polish doughnut (Sect. 2.3f) and an LFM (Sect. 2.3e) disk at various spins. We examine how electrons in equatorial trajectories in the AD around the BH are launched out of orbit due to the radiation forces. We mark that these emitted massive particles start from various radii from the axes origin and thus encounter different environments of material and radiation density each.

We make notice here of some of the "peculiar" and very interesting particle trajectories found in Fig. 16. For example, we can see cases where the absorbing material is situated at the center of the local radiation field (e.g., Fig. 16 C1, C2). We recall that, no matter the density or amount of radiation absorbed by a particle, the radiation flux, and hence the radiation force, is al-

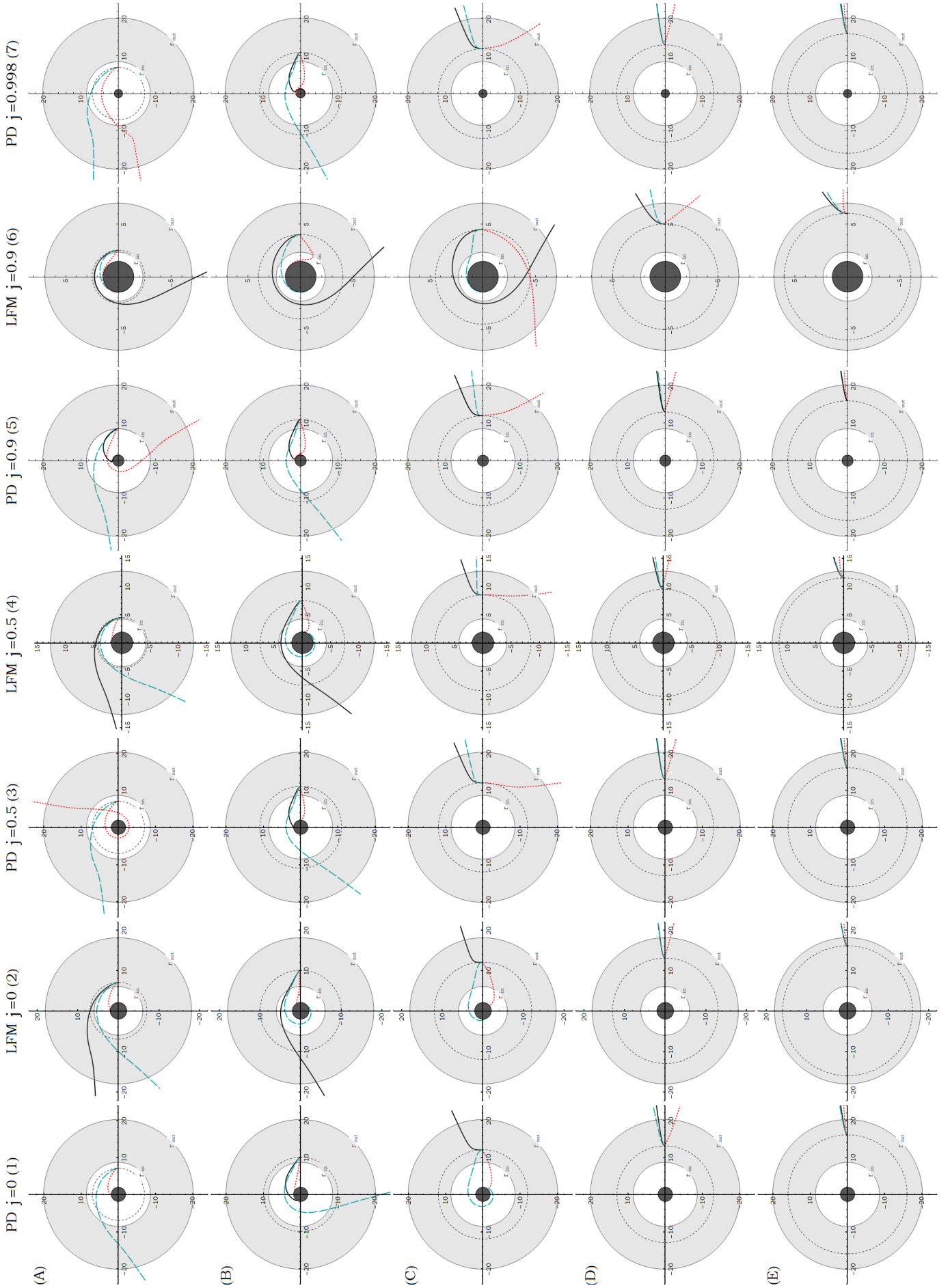


Fig. 16: Burning Arrow results: degradation of circular equatorial orbits due to the hot disk's radiation. We examine various BH spins and disk models, and record the effects of radiation on electron trajectories. In *solid black* line we have the target moving with Bardeen et al. (1972), in *dashed cyan* and in *dotted red* with MAD velocity.

Table 3: Tranquillity results and spin estimation.

Disk model	Inclin. (°)	Est. incl. (°)	Spin	Est. spin	Spin error (%)
disk	15	16.	0.13	0.13	2
disk	72	72.	0.49	0.49	0
slab	9	9.	0.06	0.07	8
slab	79	79.	0.25	0.24	3
wedge	11	11.	0.39	0.39	0
wedge	86	86.	0.4	0.39	3
torus	39	39.	0.12	0.14	13
torus	64	64.	0.32	0.32	0
ORST	80	84.8	0.41	0.41	1
ORST	82	86.3	0.86	0.81	7
PD	15	14.9	0.98	0.98	0
PD	48	47.5	0.75	0.76	1

Notes. System properties that could be retrieved from observation-like images. We see the results for a sample of random parameter executions for all disk models. The AD inclination relative to the line of sight is adequately estimated by Tranquillity. Using this information in conjunction with the divergence plots created by the code, we have an estimation of the BH spin. The spin assessment results appear to be a satisfactory approximation of the true BH spin.

ways a direct aftermath of the anisotropy of the radiation field (see e.g., Rybicki & Lightman 1986). Namely, no matter its intensity, if the radiation is isotropic, the radiation force is zero.

This has notable consequences, particularly when we examine particle motion in the local center of radiation. At such points, the radiation field is as close to isotropic as it can get for a moving target. This means that any deviation from the circular orbit (Eq. 10), even a small one, results in the test particle getting into more and more anisotropic radiation regions. This makes orbits of this sort more and more unstable, since larger radiation forces are exerted. Trajectories with such an evolution thus get rapidly out of balance and the moving particle is either slingshot outward or rapidly cross the event horizon (e.g., when following velocity models such as SANE or MAD). We could thus say that the central area of radiation resembles an "unstable equilibrium point".

In addition to the above, we have cases where noteworthy changes occur onto absorbing particles and their trajectory. For example, there are cases where the particle trajectory starts from certain radiation force areas and then enters regions of stronger, softer or counterbalanced forces. Other such notable cases are those where the traveling particle crosses into areas with markedly different spacetime curvature conditions. Instances of such situations can be seen for example in Fig. 16 A5, A7, and C6. These changes then lead to the appearance of visible and noteworthy instabilities in the trajectories, altering the expected particle curve.

Furthermore, we have cases where the particle trajectory approaches and possibly crosses the BH static limit, entering into the ergosphere (e.g., Fig. 16 B5-B7). This forces the particles under examination to change their rotation trend and follow the rotation of the central BH, as expected.

Finally, we can examine the possible extensions of the Burning Arrow code. Further applications onto the particle trajectory adjustments due to the dynamical effects in the system should be considered and looked into. For example, as suggested by the force calculations, there are indications of the initial steps of charge separation. This is because of the braking or accelerating forces exerted onto the material electrons. Since, however,

a charge separation does not occur in the disk, we can examine the electrical effects taking place inside the material. Additionally, since we have the development of ring currents within the matter, further research should be made on the ensuing magnetic phenomena and how they could influence the material motion and equilibrium. Moreover, due to the aforesaid radiation forces altering the electron orbits and motion, a survey could be conducted onto the turbulence brought on by the radiation. Ultimately, when examining the outer sections of the disk material, we notice that radiative accelerations appear stronger, while electrical binding appears weaker. Hence, in these areas, an electron orbit displacement is more likely to temporarily appear. In such a case, the instabilities development and their ramifications for the magnetorotational instability and magnetic reconnection occurrence further out, should be looked into thoroughly.

4. Conclusions & Discussion

In this work we studied the radiation field produced by the hot accretion disk orbiting a black hole. This field proves to be eminently complicated for a number of reasons. These include the existent general relativistic effects and the radiation source geometry, which is not located at the setup's center but extends in a large azimuthal and poloidal volume of space in the periphery.

For this study we considered a broad variety of accretion disk models. Some of the models we considered are opaque, while others are quasi-opaque with diverse degrees of density gradients. For the geometrical profiles of the disks, we examined an assortment of different shapes and sizes. We thus investigated situations of different disk characteristics, such as the maximum material height and the inner disk edge. Furthermore, we adopted and applied diverse velocity profiles for the material, attempting to cover as many of the particle motion situations as possible. Moreover, we examined different disk temperature profiles, such as disks heated up by the accretion process ($T \propto r^{-3/4}$) and isothermal disks. We note, however, that the codes created are highly adaptable and modifiable (publicly available, links in Acknowledgements or Koutsantoniou 2022). This means that adjustments and expansions can be made in order to accommodate any related research required for configurations in such spacetime conditions or in relevant arrangement setups.

A short summary of the research and results presented in this study is as follows. The Omega code and its multitude of generations gave results about massless and massive particle trajectories in the vicinity of compact objects. These objects affect and modify the spacetime form and structure around them in numerous ways. We can thus observe particle or bundle trajectories following the spacetime curvature and rotation. Subsequently, we used the Infinity code and thoroughly researched the radiation field created by the hot accretion disk orbiting an astrophysical black hole. Later on, we studied images of such setups from far away using the Elysium code. We scrupulously looked into the depiction results and attempted to locate the type of information we could draw for the configuration from each of the figures. This led to the development of the Tranquillity code. This algorithm collects arrangement depiction information and creates inclination - divergence plots. These plots are later on used as a scale, providing an estimation of the spin of random environments of black holes encircled by accretion disks. So far, the results of the spin conjecture appear to be good approximations of the real spin of the compact objects. Finally, we investigated the repercussions of the disk's thermal radiation onto the disk material itself. For this purpose we used the Burning Arrow

code and examined the destabilized trajectories followed by the disk electrons absorbing the high energy light.

This work is novel in the sense that for the first time, to our knowledge, the radiation field created by the accretion disk orbiting a black hole is extensively studied, measured and depicted. This field is computationally calculated in a large volume of space for many configurations inward, outward and if possible, inside the accretion disk itself. Additionally, the radiation created is examined in the vicinity of notable system areas, such as the disk's edges, the material outflow and inflow regions, the ergosphere, the event horizon, and more. A broad quantity of numerical results, images, and plots has been produced and can be surveyed for many purposes.

The numerical results of this study showed that optically thick accretion tori are more efficient in producing radiation forces for the material, as expected. Semi-opaque tori can however approach this limit under certain conditions. The results show that the primary factor affecting the radiation forces recorded appears to be the density gradient. Namely, considering disks with comparable structures, we see that the faster the material density increases, the larger the radiation forces exerted are. We clarify here that the quasi-opaque disks we used for this research are not tenuous. Their number density promptly rises to optical depth $\tau \geq 1$ and thus we anticipate limited radiation losses due to a possibly smaller effective source extent. Furthermore, we observed opaque disk models of small volume recording higher radiation forces than significantly more voluminous quasi-opaque disks with optical depths $\tau \sim 1 - 5$. We thus consider the primary factor influencing the recorded radiation forces to be the material density increase rate and not the volume occupied by the disk material.

Also, we observed the anticipated stronger radiation forces when the torus maximum height increases. Comparisons between various disk models can additionally reveal particular properties of each model. For example, we notice that for the outflow-jet regions, polish doughnuts (PD) and rotationally supported disks (ORST) record far larger radiation forces than the rest of the models. Specifically, for lower spins a where ORST is rather small-scale, PD prevails on radiation forces exerted. On the contrary, for larger spins, ORST disks are more voluminous. This fact, in conjunction with the material full opacity results in larger outflow forces being noted by ORST disks for larger spins. Additionally, concerning the two aforementioned models we notice that for medium spins $a \approx 0.5M$, rather large forces were recorded to be exerted onto halo free particles. This merits a closer investigation in order to be confirmed and, if so, a further inquiry on the reasons causing the phenomenon.

Continuing further on, we notice the intense radiation force predominance of the ORST disk for very high spins. This is, however, overturned for LFM disk targets with the "main disk" velocity. This is anticipated, since for that disk and velocity profile the material rotates faster and closer to the event horizon. When, nonetheless, we examine softer material motion such as SANE or MAD, the rotational velocities are smaller and the ORST disk recaptures the leading position in radiation forces. Continuing on, a quick comparison between the opaque disk models considered reveals that the Torus model records the highest radiation force magnitude in the majority of cases. This is also anticipated since it is the most voluminous configuration between the opaque models. Apposing the above with a comparison between the large semi-opaque LFM disk and the smaller opaque disk results also upholds the aforesaid hypothesis. That hypothesis is that the primary factor deciding the radia-

tion forces' impact onto the disk material is primarily the density gradient and not the disk volume.

Numerous parts of our work reveal that the effects of the thermal radiation onto the disk material itself are significant and should not be overlooked as inconsequential. This radiation proves to be larger and stronger than anticipated and creates noticeable accelerations, positively not negligible. Even though as mentioned earlier these radiation forces act upon the material electrons, they undoubtedly exert forces onto the disk protons as well, even indirectly. Radiation thus results in material orbit destabilizations that affect the accretion process. These destabilizations could be in the form of turbulence, magnetorotational instability or any other sort of instability. Depending on the destabilization area characteristics and properties, these processes can then lead to episodic events of matter accretion or expulsion. In a particularly interesting situation, the electron motion change leads to the formulation of electromagnetic effects, such as an electric ring current and an ensuing battery mechanism. Depending then on the material's magnetic Prandtl number and magnetic diffusion, this battery mechanism can be of varying efficiencies. The cases where the magnetic field becomes strong enough to induce notable changes and further instabilities should be thus looked into attentively.

Another matter worth looking further into is the consequences of these significant radiation forces on the dynamics and the stability of the disk itself. The modifications brought upon are noteworthy, since long considered concepts such as the ISCO must take radiation effect corrections into account.

An additional subject worth examining in the future is the radiation effects and possible repercussions on outflowing material close to the object's rotation axis. For instance, we could investigate the ramifications of radiation onto the very early stages of material outward movement, which from our current results seem appreciable. Additionally, the radiation density plots we show here demonstrate the accretion disk radiation promotes an early collimating tendency to the jet material. Finally, something that could be considered in the future is how the calculated radiation affects more complex situations, such as the disk evolution in X-ray binaries and the observed hardness-intensity diagrams.

Acknowledgements. The author would like to thank Stavros Dimitrakoudis, Dimitrios Millas, and George Pappas for their very useful questions and comments. The author would also like to express gratitude to the anonymous referees of Part I and Part II of this work for their valuable suggestions and guidance. This work was in part supported by the General Secretariat for Research and Technology of Greece and the European Social Fund in the framework of Action "Excellence". Part of this work was performed at the Research Center for Astronomy and Applied Mathematics of the Academy of Athens. The algorithms discussed in this work can be found here: Omega: <https://gitlab.com/leelamichaels/Omega.git>
Infinity: <https://gitlab.com/leelamichaels/Infinity.git>
Elysium: <https://gitlab.com/leelamichaels/Elysium.git>
Tranquillity: <https://gitlab.com/leelamichaels/Tranquillity.git>
Burning Arrow: https://gitlab.com/leelamichaels/Burning_Arrow.git

References

- Abbott, B. P., Abbott, R., Abbott, T. D., et al. 2020, ApJ, 892, L3
 Abramowicz, M., Jaroszynski, M., & Sikora, M. 1978, A&A, 63, 221
 Abramowicz, M. A., Chen, X. M., Granath, M., & Lasota, J. P. 1996, ApJ, 471, 762
 Abramowicz, M. A., Czerny, B., Lasota, J. P., & Szuszkiewicz, E. 1988, ApJ, 332, 646
 Abramowicz, M. A., Ellis, G. F. R., & Lanza, A. 1990, ApJ, 361, 470
 Abramowicz, M. A. & Fragile, P. C. 2013, Living Reviews in Relativity, 16, 1
 Asada, K., Nakamura, M., & Pu, H.-Y. 2016, ApJ, 833, 56
 Bardeen, J. M. 1970, ApJ, 162, 71
 Bardeen, J. M., Press, W. H., & Teukolsky, S. A. 1972, ApJ, 178, 347

- Belloni, T. 2010a, *The Jet Paradigm*, Vol. 794
- Belloni, T. M. 2010b, arXiv e-prints, arXiv:1007.5404
- Belloni, T. M. 2010c, in *Lecture Notes in Physics*, Berlin Springer Verlag, ed. T. Belloni, Vol. 794, 53
- Beloborodov, A. M. 1998, *MNRAS*, 297, 739
- Beloborodov, A. M. 1999, in *Astronomical Society of the Pacific Conference Series*, Vol. 161, *High Energy Processes in Accreting Black Holes*, ed. J. Poutanen & R. Svensson, 295
- Beloborodov, A. M. 2001, *Advances in Space Research*, 28, 411
- Bini, D., de Felice, F., & Gerialico, A. 2011a, *Classical and Quantum Gravity*, 28, 225012
- Bini, D., Gerialico, A., Jantzen, R. T., & Semerák, O. 2015, *MNRAS*, 446, 2317
- Bini, D., Gerialico, A., Jantzen, R. T., Semerák, O., & Stella, L. 2011b, *Classical and Quantum Gravity*, 28, 035008
- Bini, D., Jantzen, R. T., & Stella, L. 2009, *Classical and Quantum Gravity*, 26, 055009
- Blandford, R. D. & Narayan, R. 1992, *ARA&A*, 30, 311
- Blandford, R. D. & Znajek, R. L. 1977, *MNRAS*, 179, 433
- Bombaci, I. 1996, *A&A*, 305, 871
- Bonafede, A., Feretti, L., Murgia, M., et al. 2010, *A&A*, 513, A30
- Bozza, V. 2010, *General Relativity and Gravitation*, 42, 2269
- Broderick, A. E. & Loeb, A. 2005, *MNRAS*, 363, 353
- Carilli, C. L. & Taylor, G. B. 2002, *ARA&A*, 40, 319
- Chandrasekhar, S. 1983, *The mathematical theory of black holes*
- Christodoulou, D. M., Gabuzda, D. C., Knuettel, S., et al. 2016, *A&A*, 591, A61
- Contopoulos, I., Christodoulou, D. M., Kazanas, D., & Gabuzda, D. C. 2009, *ApJ*, 702, L148
- Contopoulos, I. & Kazanas, D. 1998, *ApJ*, 508, 859
- Contopoulos, I., Kazanas, D., & Christodoulou, D. M. 2006, *ApJ*, 652, 1451
- Contopoulos, I., Nathanail, A., & Katsanikas, M. 2015, *ApJ*, 805, 105
- Davelaar, J., Bronzwaer, T., Kok, D., et al. 2018, *Computational Astrophysics and Cosmology*, 5, 1
- Done, C., Gierliński, M., & Kubota, A. 2007, *A&A Rev.*, 15, 1
- Dubus, G. 2003, in *EAS Publications Series*, Vol. 7, *EAS Publications Series*, ed. C. Motch & J.-M. Hameury, 283
- El-Badry, K., Seeburger, R., Jayasinghe, T., et al. 2022, *MNRAS*, 512, 5620
- Esin, A. A., McClintock, J. E., & Narayan, R. 1997, *ApJ*, 489, 865
- Event Horizon Telescope Collaboration. 2019a, *ApJ*, 875, L1
- Event Horizon Telescope Collaboration. 2019b, *ApJ*, 875, L4
- Event Horizon Telescope Collaboration. 2019c, *ApJ*, 875, L6
- Event Horizon Telescope Collaboration. 2021a, *ApJ*, 910, L12
- Event Horizon Telescope Collaboration. 2021b, *ApJ*, 910, L13
- Event Horizon Telescope Collaboration. 2022a, *ApJ*, 930, L12
- Event Horizon Telescope Collaboration. 2022b, *ApJ*, 930, L13
- Event Horizon Telescope Collaboration. 2022c, *ApJ*, 930, L14
- Event Horizon Telescope Collaboration. 2022d, *ApJ*, 930, L15
- Fuerst, S. V. 2006, PhD thesis, Mullard Space Science Laboratory, University College London, Holmbury St. Mary, Dorking, Surrey RH5 6NT, UK
- Fuerst, S. V. & Wu, K. 2004, *A&A*, 424, 733
- Fuerst, S. V. & Wu, K. 2007, *A&A*, 474, 55
- Gabuzda, D. 2006, in *Proceedings of the 8th European VLBI Network Symposium*, ed. W. Baan, R. Bachiller, R. Booth, P. Charlot, P. Diamond, M. Garrett, X. Hong, J. Jonas, A. Kus, F. Mantovani, A. Marecki, H. Olofsson, W. Schlueter, M. Tomikowski, N. Wang, & A. Zensus, 11
- Gabuzda, D. C. 2015, in *Astrophysics and Space Science Library*, Vol. 414, *The Formation and Disruption of Black Hole Jets*, ed. I. Contopoulos, D. Gabuzda, & N. Kylafis, 117
- Gabuzda, D. C., Christodoulou, D. M., Contopoulos, I., & Kazanas, D. 2012, in *Journal of Physics Conference Series*, Vol. 355, *Journal of Physics Conference Series*, 012019
- Gabuzda, D. C., Knuettel, S., & Bonafede, A. 2015a, *A&A*, 583, A96
- Gabuzda, D. C., Knuettel, S., & Reardon, B. 2015b, *MNRAS*, 450, 2441
- Gabuzda, D. C., Murray, É., & Cronin, P. 2004, *MNRAS*, 351, L89
- Gabuzda, D. C., Reichstein, A. R., & O'Neill, E. L. 2014, *MNRAS*, 444, 172
- Gabuzda, D. C., Vitrichchak, V. M., Mahmud, M., & O'Sullivan, S. P. 2008, *MNRAS*, 384, 1003
- Govoni, F., Dolag, K., Murgia, M., et al. 2010, *A&A*, 522, A105
- Herrnstein, J. R., Moran, J. M., Greenhill, L. J., & Trotter, A. S. 2005, *ApJ*, 629, 719
- Hovatta, T., Aller, M. F., Aller, H. D., et al. 2014, *AJ*, 147, 143
- Hovatta, T., Lister, M. L., Aller, M. F., et al. 2012, *AJ*, 144, 105
- Hughes, S. A. 2005, arXiv e-prints, hep
- Igumenshchev, I. V., Narayan, R., & Abramowicz, M. A. 2003, *ApJ*, 592, 1042
- Jayasinghe, T., Stanek, K. Z., Thompson, T. A., et al. 2021, *MNRAS*, 504, 2577
- Kaloga, V. & Baym, G. 1996, *ApJ*, 470, L61
- Kerr, R. P. 1963, *Phys. Rev. Lett.*, 11, 237
- Koljonen, K. I. I., Hannikainen, D. C., McCollough, M. L., Pooley, G. G., & Trushkin, S. A. 2010, *MNRAS*, 406, 307
- Komissarov, S. S. 2001, *MNRAS*, 326, L41
- Koutsantoniou, L. E. 2022, *A&A*, 657, A32
- Koutsantoniou, L. E. & Contopoulos, I. 2014, *ApJ*, 794, 27
- Kozłowski, M., Jaroszynski, M., & Abramowicz, M. A. 1978, *A&A*, 63, 209
- Krause, M. & Lühr, A. 2004, *A&A*, 420, 115
- Kronberg, P. P., Dufton, Q. W., Li, H., & Colgate, S. A. 2001, *ApJ*, 560, 178
- Kylafis, N. D., Contopoulos, I., Kazanas, D., & Christodoulou, D. M. 2012, *A&A*, 538, A5
- Lamb, F. K. & Miller, M. C. 1995, *ApJ*, 439, 828
- Larmor, J. 1917, *Nature*, 99, 404
- Lasota, J. P. 1999, *Phys. Rep.*, 311, 247
- Lasota, J.-P. 2016, in *Astrophysics and Space Science Library*, Vol. 440, *Astrophysics of Black Holes: From Fundamental Aspects to Latest Developments*, ed. C. Bambi, 1
- Levin, J. & Grossman, R. 2009, *Phys. Rev. D*, 79, 043016
- Levin, J. & Perez-Giz, G. 2008, *Phys. Rev. D*, 77, 103005
- Livio, N., Ogilvie, G. I., & Pringle, J. E. 1999, *ApJ*, 512, 100
- Mahmud, M., Coughlan, C. P., Murphy, E., Gabuzda, D. C., & Hallahan, D. R. 2013, *MNRAS*, 431, 695
- Mahmud, M. & Gabuzda, D. 2007, in *From Planets to Dark Energy: the Modern Radio Universe*, 74
- Mahmud, M. & Gabuzda, D. C. 2008, in *Astronomical Society of the Pacific Conference Series*, Vol. 386, *Extragalactic Jets: Theory and Observation from Radio to Gamma Ray*, ed. T. A. Rector & D. S. De Young, 494
- Mahmud, M., Gabuzda, D. C., & Bezrukovs, V. 2009, *MNRAS*, 400, 2
- McKinney, J. C. 2005, *ApJ*, 630, L5
- Miller, M. C. & Lamb, F. K. 1993, *ApJ*, 413, L43
- Miller, M. C. & Lamb, F. K. 1996, *ApJ*, 470, 1033
- Misner, C. W., Thorne, K. S., & Wheeler, J. A. 1973, *Gravitation*
- Mościbrodzka, M., Falcke, H., Shiokawa, H., & Gammie, C. F. 2014, *A&A*, 570, A7
- Murphy, E., Cawthorne, T. V., & Gabuzda, D. C. 2013, *MNRAS*, 430, 1504
- Murphy, E. & Gabuzda, D. 2013, in *European Physical Journal Web of Conferences*, Vol. 61, *European Physical Journal Web of Conferences*, 07005
- Nakamura, M., Asada, K., Hada, K., et al. 2018, *ApJ*, 868, 146
- Narayan, R. & Bartelmann, M. 1996, arXiv e-prints, astro
- Narayan, R., Igumenshchev, I. V., & Abramowicz, M. A. 2003, *PASJ*, 55, L69
- Narayan, R. & McClintock, J. E. 2008, *New A Rev.*, 51, 733
- Narayan, R., Sądowski, A., Penna, R. F., & Kulkarni, A. K. 2012, *MNRAS*, 426, 3241
- Narayan, R. & Yi, I. 1994, *ApJ*, 428, L13
- Narayan, R. & Yi, I. 1995, *ApJ*, 444, 231
- Noble, S. C., Leung, P. K., Gammie, C. F., & Book, L. G. 2007, *Classical and Quantum Gravity*, 24, S259
- Novikov, I. D. & Thorne, K. S. 1973, in *Black Holes (Les Astres Occlus)*, 343–450
- O'Sullivan, S. P. & Gabuzda, D. C. 2009, *MNRAS*, 393, 429
- Page, L. 1918, *Physical Review*, 11, 376
- Park, J., Hada, K., Kino, M., et al. 2019, *ApJ*, 871, 257
- Penna, R. F., Sądowski, A., Kulkarni, A. K., & Narayan, R. 2013, *MNRAS*, 428, 2255
- Penrose, R. & Floyd, R. M. 1971, *Nature Physical Science*, 229, 177
- Podsiadlowski, P., Rappaport, S., & Pfahl, E. D. 2002, *ApJ*, 565, 1107
- Poynting, J. H. 1903, *MNRAS*, 64, A1
- Refsdal, S. 1964, *MNRAS*, 128, 295
- Reichstein, A. & Gabuzda, D. 2012, in *Journal of Physics Conference Series*, Vol. 355, *Journal of Physics Conference Series*, 012021
- Reig, P. & Fabregat, J. 2015, *A&A*, 574, A33
- Reig, P., Nersesian, A., Zezas, A., Gkouvelis, L., & Coe, M. J. 2016, *A&A*, 590, A122
- Robertson, H. P. 1937, *MNRAS*, 97, 423
- Rybicki, G. B. & Lightman, A. P. 1986, *Radiative Processes in Astrophysics* (Wiley-VCH)
- Sadowski, A. 2011, arXiv e-prints, arXiv:1108.0396
- Sauer, T. 2008, *Archive for History of Exact Sciences*, 62, 1
- Shakura, N. I. & Sunyaev, R. A. 1973, *A&A*, 500, 33
- Sądowski, A. 2009, *ApJS*, 183, 171
- Tauris, T. M. & van den Heuvel, E. P. J. 2006, in *Compact stellar X-ray sources*, Vol. 39, 623–665
- Taylor, G. B. & Zavalá, R. 2010, *ApJ*, 722, L183
- Tetarenko, B. E., Sivakoff, G. R., Heinke, C. O., & Gladstone, J. C. 2016, *ApJS*, 222, 15
- Thompson, T. A., Kochanek, C. S., Stanek, K. Z., et al. 2019, *Science*, 366, 637
- Thorne, K. S. & Price, R. H. 1975, *ApJ*, 195, L101
- Tsvetanov, Z. I., Allen, M. G., Ford, H. C., & Harms, R. J. 1999, in *The Radio Galaxy Messier 87*, ed. H.-J. Röser & K. Meisenheimer, Vol. 530, 301
- Uttley, P., McHardy, I. M., & Vaughan, S. 2005, *MNRAS*, 359, 345
- van der Klis, M. 1995, in *NATO Advanced Study Institute (ASI) Series C*, Vol. 450, *The Lives of the Neutron Stars*, ed. M. A. Alpar, U. Kiziloglu, & J. van Paradijs, 301
- van der Klis, M. 2004, arXiv e-prints, astro
- van der Klis, M. & Bonnet-Bidaud, J. M. 1989, *A&A*, 214, 203
- Widrow, L. M. 2002, *Reviews of Modern Physics*, 74, 775
- Wilkins, D. C. 1972, *Phys. Rev. D*, 5, 814
- Wu, K., Ball, W., & Fuerst, S. V. 2008a, arXiv e-prints, arXiv:0811.2060
- Wu, K., Fuerst, S. V., Mizuno, Y., et al. 2008b, *Chinese Journal of Astronomy and Astrophysics Supplement*, 8, 226
- Younsi, Z. 2014, PhD thesis, UCL, United Kingdom
- Younsi, Z., Wu, K., & Fuerst, S. V. 2012, *A&A*, 545, A13
- Zavalá, R. T. & Taylor, G. B. 2002, *ApJ*, 566, L9
- Zavalá, R. T. & Taylor, G. B. 2003, *ApJ*, 589, 126
- Zavalá, R. T. & Taylor, G. B. 2004, *ApJ*, 612, 749
- Zavalá, R. T. & Taylor, G. B. 2005, *ApJ*, 626, L73
- Zhang, S. N., Cui, W., & Chen, W. 1997, *ApJ*, 482, L155